Spectral tracks in the ionosphere: Fast Fourier Transform analysis of seismo- ionospheric coupling through GPS Total Electron Content variations

Secil Karatay
skaratay@kastamonu.edu.tr

Kastamonu University
Ali Cinar
Kastamonu University
Feza Arikan
Hacettepe University
Orhan Arikan
Bilkent University

Research Article

Keywords: Seismo-ionospheric coupling, GPS-TEC, Fast Fourier Transform, ionospheric precursors, GNSS monitoring

Posted Date: August 14th, 2025

DOI: https://doi.org/10.21203/rs.3.rs-7186871/v1

Additional Declarations: No competing interests reported.

Version of Record: A version of this preprint was published at Tectonophysics on May 5th, 2026. See the published version at https://doi.org/10.1016/j.tecto.2026.231240.

Spectral tracks in the ionosphere: Fast Fourier Transform analysis of seismo-ionospheric coupling through GPS Total Electron Content variations

Secil Karatay[1](corresponding author), Ali Cinar[1], Feza Arikan[2], Orhan Arikan[3]

[1]Kastamonu University, Department of Electrical Electronics Engineering, 37150 Kastamonu, Türkiye
skaratay@kastamonu.edu.tr, acinar@kastamonu.edu.tr

[2]Hacettepe University, Department of Electrical Electronics Engineering, 06800 Ankara, Türkiye
arikan@hacettepe.edu.tr

[3]Bilkent University, Department of Electrical Electronics Engineering, 06800 Ankara, Türkiye
oarikan@bilkent.edu.tr

Abstract

This study investigates the relationship between ionospheric disturbances and seismic activity through spectral analysis of Total Electron Content (TEC) variations. Using a specialized Fast Fourier Transform algorithm (IONOLAB-FFT), we analyze TEC data from dense GNSS networks across thirteen significant earthquakes (Mw 5.6-9.0) in diverse tectonic settings, including nine world events and four in Türkiye. Our analysis reveals consistent spectral patterns preceding earthquakes, characterized by systematic shifts toward lower dominant frequencies, narrowing bandwidths, and increasing durations as seismic events approach. These patterns show strong magnitude dependence, with major earthquakes ($Mw \geq 8.0$) exhibiting dominant frequencies of 0.3-0.4 mHz and detectable ionospheric anomalies 4-5 days before the main shock, while moderate events (Mw 6.0-7.0) display higher frequencies (0.7-0.8 mHz) with precursors evident only 1-2 days prior. Notably, pre-earthquake ionospheric signatures progressively transform from patterns resembling geomagnetically quiet conditions to those characteristic of disturbed periods, despite the absence of significant geomagnetic activity. Frequency-duration relationships demonstrate increasingly strong negative correlations as earthquakes approach, with spatial analysis showing clear epicentral focusing of anomalies. Comparative assessment between world and Türkiye earthquakes reveals both universal patterns and region-specific characteristics, with Türkiye events showing somewhat shorter precursory signal detection times despite similar magnitude-dependent trends. Secondary frequency peaks emerge 2-3 days before major events, potentially indicating different phases of the preparation process. The consistent patterns identified across diverse tectonic settings suggest that ionospheric precursors reflect fundamental physical processes related to pre-seismic strain accumulation. This research provides a quantitative framework for characterizing seismo-ionospheric coupling, offering potential applications for earthquake early warning systems through electromagnetic precursor monitoring.

Keywords Seismo-ionospheric coupling · GPS-TEC · Fast Fourier Transform · ionospheric precursors · GNSS monitoring

Introduction

One of the most impressive areas of geophysics and space weather research is the complex relation between ionospheric disturbances and seismic activity (Karatay, et al., 2010; Shi, et al., 2021; Adil, et al., 2022; Karatay & Gul, 2023; Qingshan Ruan, et al., 2023; Budak, et al., 2024; Tachema, 2024; Luhrmann, et al., 2025). Over the past few decades, seismo-ionospheric disturbances, which are characterized as abnormal variations in ionospheric parameters that are temporally and geographically related to earthquake preparation and occurrence, have attracted a lot of scientific attention (Ondoh, 2000; Jin, et al., 2014; Jing, et al., 2022; Li, et al., 2024). Various physical phenomena, including Radon emission and electromagnetic variations, undergo significant variations as a result of fault ruptures preceding an earthquake. The fracturing of rocks can lead to the release of gases like Radon into the atmosphere (King, 1986; Igarashi, et al., 1995; Trique, et al., 1999; Pulinets & Ouzounov, 2011). Moreover, the stress and strain associated with fault activity can influence the Earth's electromagnetic environment, triggering ionospheric anomalies and disturbances that are detectable through both satellite-based and ground-based monitoring systems (Pulinets, 2004; Gousheva, et al., 2008; Fan, et al., 2015; Novikov & Sorokin, 2024). These disturbances show up as variations in the distribution of ionospheric electron density, which may be observable days to hours before significant seismic occurrences. This suggests that they could be useful as early warning systems and earthquake prediction precursors.

The ionosphere, extending approximately from 60 km to 1000 km above Earth's surface, is a natural screen that reacts to a variety of geophysical events, including lithospheric activity. A variety of physical processes, such as Acoustic Gravity Waves (Rapoport, et al., 2004; Kaladze, et al., 2008; Mikumo & Watada, 2009), electromagnetic emissions (Molchanov, et al., 1995; Fan, et al., 2015; Chowdhury, et al., 2022), variations in atmospheric electric fields (Liperovsky, et al., 2008; Harrison, et al., 2010; Hobara, et al., 2022) and anomalous Radon emanation (Liperovsky, et al., 2005; Omori, et al., 2007; Nikolopoulos, et al., 2024) from active fault zones, are included in the hypothesized mechanisms connecting seismic events to ionospheric disturbances. These mechanisms may produce a series of consequences that lead to observable ionospheric anomalies and disturbances before and after the earthquakes.

One of the most reliable and estimatable parameter for tracking ionospheric behavior is Total Electron Content (TEC). It is the integrated electron density along a path through the ionosphere. The extensive use of Global Navigation Satellite System (GNSS) receivers offers TEC measurements previously unheard-of spatial and temporal coverage, allowing for thorough monitoring of ionospheric conditions in a variety of geographic locations (Sardón, et al., 1994; Arikan, et al., 2003; Rideout & Coster, 2006; Nayir, et al., 2007; Sezen, et al., 2013). Because of its continuous estimating capabilities and sensitivity to a variety of geophysical effects, TEC is especially useful for detecting minor pre-seismic ionospheric signals against the backdrop of typical diurnal (Yuen & Roelofs, 1966), seasonal (Yuen & Roelofs, 1967), and solar-driven variations (Lean, et al., 2016; Solomon, et al., 2018; Siddiqui, et al., 2021). TEC data can be also processed at high temporal resolutions that makes it possible to near real-time analysis of the ionospheric anomalies occuring before the seismic events (Liu, et al., 2009; Karatay, et al., 2010; Jin, et al., 2014; Su & Sha, 2022; Colonna, et al., 2023; Li, et al., 2024; Ching-Chou, et al., 2025; Karatay, et al., 2025). Machine Learning and advanced signal processingn techniques are two recent developments in GNSS-TEC processing algorithms that have greatly improved the capacity to distinguish normal ionospheric variability from earthquake-related disturbances. Combining TEC anomalies with other geophysical observations can allow for short-term earthquake forecasting, as they have occured hours or even days before significant seismic events. TEC estimates are also important for tracking space weather phenomena like solar flares, geomagnetic storms, and ionospheric scintillation as a critical parameter at the intersection of atmospheric science, geophysics and hazard mitigation (Ghafar, et al., 2024; Budak, et al., 2024; Perfetti, et al., 2025; Karatay, et al., 2025).

Although seismo-ionospheric researches have made great strides, there are still considerable handicaps in distinguishing reliable earthquake-related ionospheric anomalies from fluctuations caused by other factors such as including solar activity, geomagnetic disturbances and weather conditions. Furthermore, our comprehension of the physical origins and transmission processes of seismo-ionospheric disturbances is limited due to the lack of accurate quantification of their temporal properties and frequency components. Although empirical thresholding methods and statistical models have shown some performance in anomaly detection, they frequently fall short in distinguishing overlapping effects. The need for sophisticated signal processing techniques that can extract time, ephemeral information from TEC time series is therefore increasing. These techniques include wavelet decomposition (Naaman, et al., 2001; Borries, 2010; Amiri-Simkooei & Asgari, 2012), time-frequency analysis (Wang & Morton, 2015; Skeberis, et al., 2015; Koroglu, et al., 2020) and nonlinear dynamical systems approaches (E. R. Ackermann, 2011; Belashov & Belashova, 2015; Saleem & Shan, 2020). Furthermore, the lack of high-resolution multi-instrument observations and reliable cross-validation across various geographic locations contributes to the incomplete understanding of the spatial coherence and propagation properties of earthquake-induced ionospheric anomalies.

Fourier Transform (FT) approaches offer a potent mathematical framework that can uncover spectral characteristics and periodic patterns that could otherwise be hidden in the time domain by decomposing time-series data into its frequency components (Cooley, et al., 1969; Bracewell, 1989; Duhamel & Vetterli, 1990). Applying Fourier analysis to ionospheric TEC data covering pre-, during-, and post-earthquake periods may reveal unique spectral characteristics related to ionospheric perturbations caused by the earthquakes. These perturbations can be distinguished from other sources of ionospheric variability by their distinct spectrum morphologies, heightened power in particular frequency bands or distinctive temporal evolution patterns. With major advantages over conventional techniques in terms of computational efficiency and insight production, the Fast Fourier Transform (FFT) has become an essential analytical tool for identifing the ionospheric disturbances (Chernogor, 2008; Wang, et al., 2014; Raghunath & Ratnam, 2015; Cravens, et al., 2023). By converting TEC time series from the spatial domain to the frequency domain, FFT makes it possible to identify periodic variations, distinguish between disturbances at various wavelengths and characterize traveling ionospheric disturbances with high precision in the ionosphere (Helmboldt, et al., 2012; Danilov, 2013; Liu, et al., 2014; Kowsik, et al., 2015; Crowley, et al., 2016). There are various methodological issues in applying FFT on TEC data. Window sizes and overlaps must be carefully considered due to the non-stationary nature of ionosphere in the spectral analysis as presented in Karatay (2020a) and (2020b). The assumption of signal stationarity accepted by conventional FFT techniques is rarely true for ionospheric data that is impacted by seasonal impacts, diurnal changes and intermittent disturbances. Therefore, the existence of several spectral components throughout a range of time scales from minutes to days calls for multi-resolution techniques that can capture both quick, fleeting characteristics and more gradual, evolving patterns (Arikan & Yarici, 2017; Karatay, 2020a; Karatay, 2020b). Finally, the spatial heterogeneity of seismo-ionospheric effects necessitates the development of coherent frameworks for spatial-temporal analysis that can distinguish between local and regional disturbances and follow the propagation of anomalies.

This paper uses a specially developed spectral analysis technique, namely IONOLAB-FFT algorithm, designed especially for ionospheric disturbances researches to overcome these issues. The IONOLAB-FFT algorithm is implement with adaptive window sizing as in Karatay (2020a) and (2020b). This algorithm makes it possible to thoroughly characterize the temporal analysis and spectral content of seismo-ionospheric disturbances across several frequency bands. The analysis refers a large dataset of TEC measurements from dense GNSS networks in several seismically active regions, such as China, Japan, California, Chile, Italy, Mexico, and finally Türkiye. By covering a large number of earthquake events of different magnitudes ($Mw \geq 5.0$), depths and fault mechanisms, the dataset provides a strong basis for investigating how the spectral features of seismo-ionospheric disturbances vary with earthquake magnitudes, geomagnetic and background ionospheric conditions. The investigation focuses in particular on the temporal evolution of tracks in the ionosphere prior to and during the seismic occurrences. According to earlier studies, pre-seismic ionospheric anomalies/disturbances may have unique spectral features, such as increased power in Ultra Low Frequency (ULF) (Eftaxias, et al., 2010; Swati, et al., 2020; Hayakawa, et al., 2023) and Extremely Low Frequency (ELF) (Hayakawa, et al., 2020; Hayakawa, et al., 2023; Tritakis, et al., 2024) bands, which may be connected to electromagnetic emissions from strained rock formations. On the other hand, co-seismic effects frequently appear in higher frequency bands related to gravity and acoustic waves produced by ground motion (Reddy, et al., 2015; Marchetti, et al., 2020; Sripathi, et al., 2020; Ruan, et al., 2025). This paper aims to establish a more reliable framework for detecting pre-seismic spectral tracks in the ionosphere and differentiating them from geomagnetic ionospheric conditions by precisely describing these temporal patterns. The study is conducted in two distinct groups: one focusing on world earthquakes with magnitudes between Mw 9.0 and 5.6 and the other on four earthquakes that occurred within Türkiye with magnitudes between Mw 8.8 and 6.7. The data is estimated for separately each group, utilizing IONOLAB-TEC data obtained from International GNSS Service (IGS) stations for world earthquakes and from the Turkish National Permanent GNSS Network-Active (TNPGN-Active) stations for earthquakes in Türkiye. The identification of reliable ionospheric precursors with magnitude-dependent lead times could significantly enhance existing earthquake early warning systems, potentially providing hours to days of advanced warning compared to conventional seismic-based systems that typically offer seconds to minutes. Such extended warning periods could enable more effective emergency preparedness, population evacuation from vulnerable structures, and critical infrastructure protection in high-risk seismic zone

The following sections of this study describe the data selection criteria and geomagnetic ionospheric conditions and steps and application of IONOLAB-FFT algoritm. Evaluations of the frequency and time components observed throughout the complete dataset are offered after a thorough analysis of case studies from a variety of seismic occurrences. The algorithm is also applied to geomagnetically disturbed and quiet days periods to differantiate the seismic and geomagnetic disturbances with each other. A brief discussion of the data and the ionospheric conditions druing the chosen periods is given in Section 2. The steps of the IONOLAB-FFT algoritm is presented in Section 3. The results of applying the IONOLAB-FFT algorithm to the

GPS-TEC data obtained for geomagnetically disturbed and quiet days and ten earthquake periods are presented in Section 3.

Data and Space Weather Conditions for the Chosen Periods

This study employs the Regularized Estimation of TEC (Reg-Est) algorithm with dual-frequency CORS to calculate IONOLAB-TEC, as outlined in Arikan et al. (2003, 2004). IONOLAB-TEC utilizes the advanced Reg-Est signal processing algorithm to incorporate data from all usable satellites within the GPS receiver's local horizon (Arikan, et al., 2003; Arikan, et al., 2004; Nayir, et al., 2007; Sezen, et al., 2013). Satellite Differential Code Biases are extracted from IONEX files, while receiver DCBs are determined using the IONOLAB-BIAS algorithm (Arikan, et al., 2008). The necessary IONEX files, satellite ephemeris and satellite DCB data are sourced from NASA's CDDIS FTP server from ftp://cddis.gsfc.nasa.gov/gps/products/ionex/. For each station, IONOLAB-TEC produces 576 samples at 2.5-minute resolution (IONOLAB, 2007).

The study has been carried out under two separate groups: earthquakes that occurred in the world and earthquakes that occurred in Türkiye. Nine earthquakes with magnitudes between Mw 9.0 and 5.6 that occurred around the world are selected for the first group of the study. Four earthquakes with magnitudes between Mw 7.8 and 6.7 occurred in Türkiye chosen for the second group of the study. The IONOLAB-FFT algorithm has been also implemented in two groups of IONOLAB-TEC data estimated for five days before the earthquake (pre-earthquake period) and the earthquake days (co-earthquake periods) for each station from International GNSS Service (IGS) stations for the world earthquaekes and from Turkish National Permanent GNSS Network- Active (TNPGN-Active) stations for Türkiye earthquakes. Time, location and magnitude information of world earthquakes organized according to the magnitude are provided in Table 1 and the chosen IGS stations are shown in Fig 1 (USGS, 1879; IGS, 1994). Earthquakes information for Türkiye and chosen TNPGN-Active stations are presented in Table 2 and Fig. 2, respectively (USGS, 1879).

Table 1 Geographic location, time, magnitude and depth of the chosen world earthquakes and used GNSS station (USGS, 1879)

Earthquake (Number: Location)	Time (Day, UTC Time)	Epicenter (Latitude-Longitude)	Magnitude (Richter Mw)	Depth (km)	Stations
E1: Tohoku, Japan	11 March 2011 UTC: 05:46	38.32°N-142.36°E	9.0	29	AIRA, MTKA, MIZU, SMST, TSK2, TSKB, STK2, USUD, YSSK
E2: Maule, Chile	27 February 2010 UTC: 06:34	35.84°S-72.71°W	8.8	35	ANTC, AREQ, CFAG, CONZ, COPO, COYQ, IQQE, LPGS, SANT, UNSA
E3: Wenchuan, China	12 May 2008 UTC: 06:28	31.02°N-103.36°E	7.9	19	CHAN, DAEJ, GUAO, KUNM, LHAZ, SHAO, SUWN, TCMS, XIAN
E4: Oaxaca, Mexican	23 June 2020 UTC: 15:29	15.93°N-95.93°W	7.4	20	GUAT, INEG, MANA, RDSD, SSIA,
E5: California, USA	04 April 2010 UTC :22:40	32.13°N-115.30°W	7.2	10	BLYT, CRFP, DHLG, GOL2, MONP, PIN1, TRAK
E6: Iwate, Japan	13 June 2008 UTC: 23:43	39.01°N-140.52°E	6.9	8	AIRA, MTKA, MIZU, SMST, TSK2, TSKB, STK2, USUD, YSSK
E7: Yushu, China	14 April 2010 UTC: 23:49	33.16°N-96.62°E	6.9	17	CHAN, DAEJ, GUAO, KUNM, LHAZ, SHAO, SUWN, TCMS, XIAN
E8-E9: Norcia, Italy	24 August 2016 UTC: 01:36-02:33	42.71°N-13.17°E 42.79°N-13.15°E	6.2 5.6	10 10	BZRG, GENO, IENG, IGMİ, MAT1, MATE, MEDI

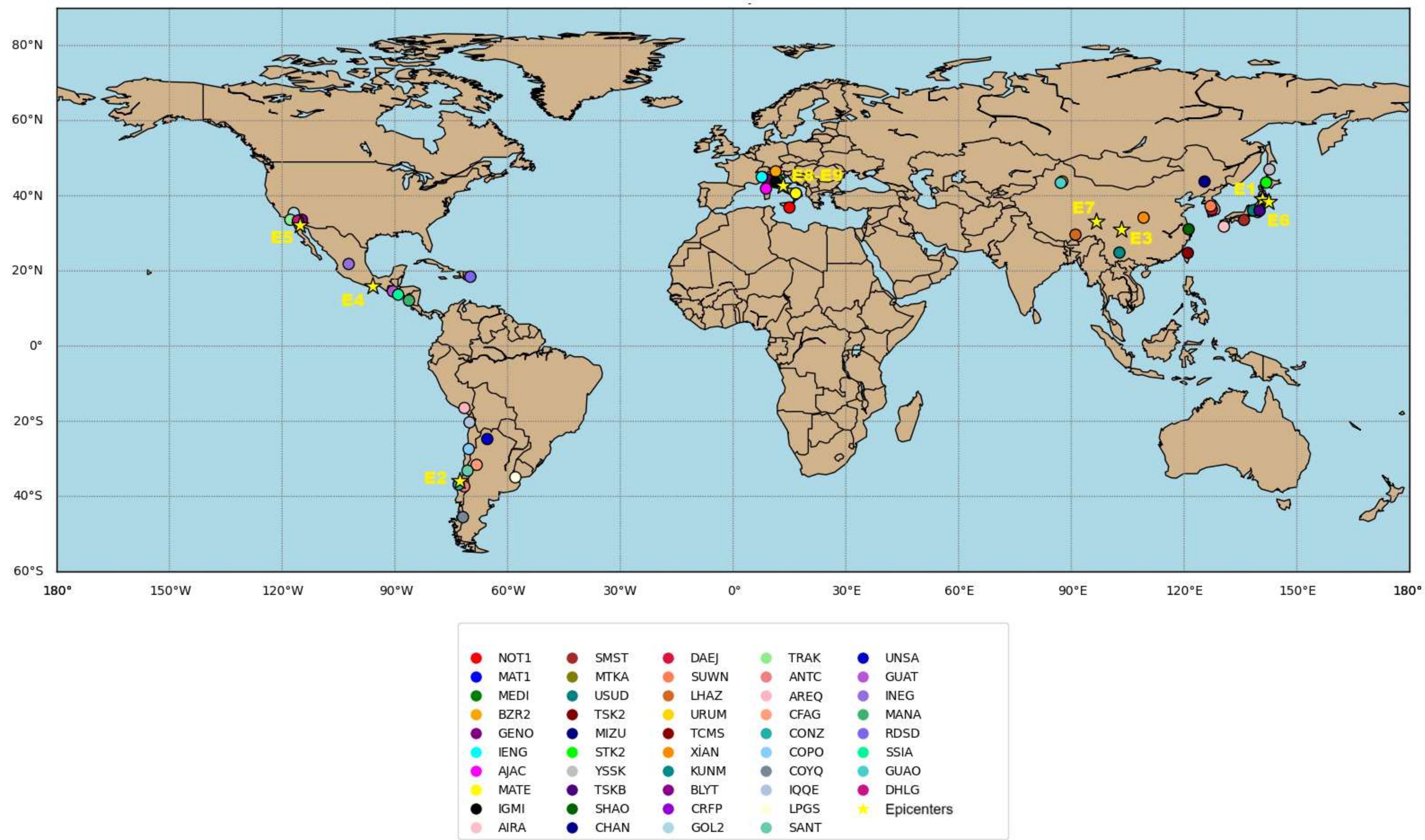

Fig. 1 Location of GNSS stations used for the world earthquakes and the epicenters (IGS, 1994; USGS, 1879)

Table 2 Date, occurring time, geographic locations magnitude and depth of the Türkiye earthquakes

Earthquake (Number: Location)	**Time (Day, UTC Time)**	**Latitude (°N)**	**Longitude (°E)**	**Magnitude (Richter Mw)**	**Depth (km)**
TE1: Elazığ, Türkiye	01 January 2020 UTC: 17:55	38.37	39.10	6.7	10
TE2: İzmir, Türkiye	30 October 2020 UTC: 11:51	37.89	26.79	7.0	21
TE3: Kahramanmaraş, Türkiye	06 February 2023 UTC: 01.17	37.11	37.11	7.8	17.9
TE4: Kahramanmaraş, Türkiye	06 February 2023 UTC: 10.24	38.02	37.20	7.5	10

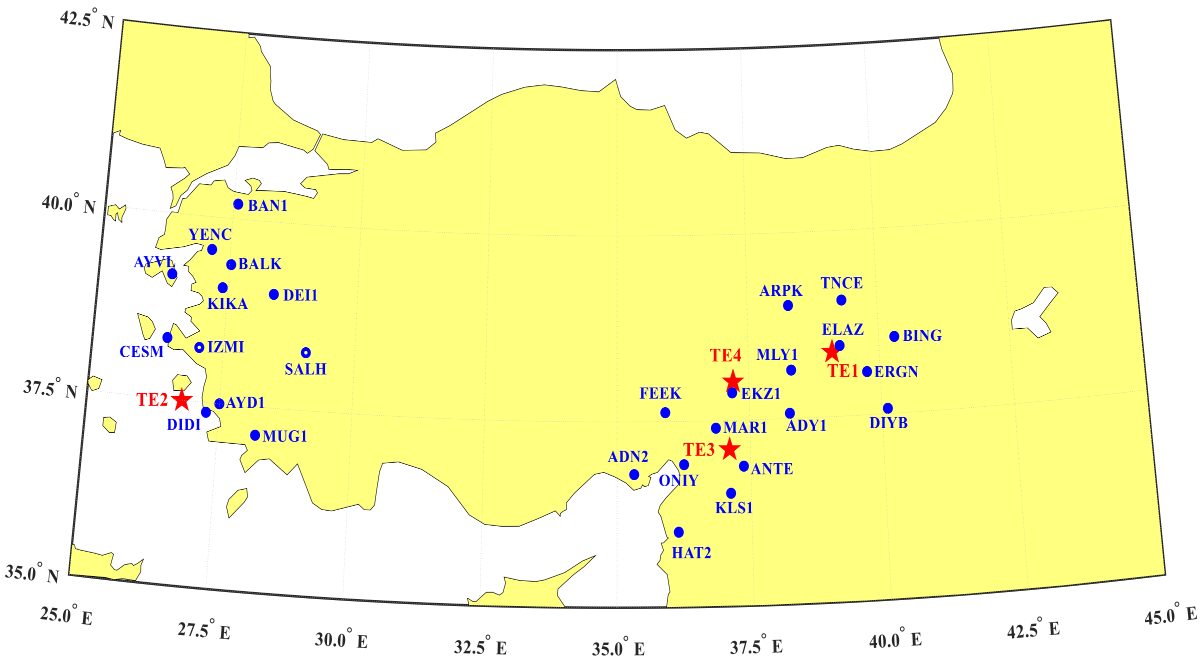

Fig. 2 Geographic location of the TNPGN-Active stations and the Türkiye earthquakes (USGS, 1879)

In order to distinguish pre-seismic disturbances from geomagnetic disturbances, IONOLAB-TEC estimates for one disturbed day are also obtained for of each earthquake year for each station. In addition, IONOLAB-TEC estimates are obtained for one geomagnetically quiet day of each earthquake year for each station. The values obtained for the quiet periods are used as threshold values for distinguishing the disturbed periods. In Table 3, investigation periods are provided both for the world earthquakes and Türkiye earthquakes. Maximum values of the daily geomagnetic indices for quiet and disturbed periods are shown for both two groups in Fig. 3. Kp and Ap values are provided from GFZ Helmholtz Centre for Geosciences and Dst values are obtained from World Data Center for Geomagnetism, Kyoto (GFZ, 1956; WDC, 1957).

Table 3 Earthquake, disturbed and quiet periods used in the study

	pre-seismic and co-earthquake periods	disturbed periods	quiet periods
E1	06-11 March 2011	05 August 2011	26 May 2011
E2	22-27 February 2010	05 April 2010	08 May 2010
E3	07-12 May 2008	27 March 2008	01 January 2008
E4	18-23 June 2020	28 September 2020	02 March 2020
E5	30-March-04 April 2010	05 April 2010	04 March 2010
E6	08-13 June 2008	04 September 2008	20 September 2008
E7	09-14 April 2010	05 April 2010	08 May 2010
E8-E9	19-24 August 2016	02 September 2016	06 November 2016
TE1	19-24 January 2020	24 April 2023	17 February 2022
TE2	25-30 October 2020	24 April 2023	17 February 2022
TE3	01-06 February 2023	24 April 2023	17 February 2022
TE4	01-06 February 2023	24 April 2023	17 February 2022

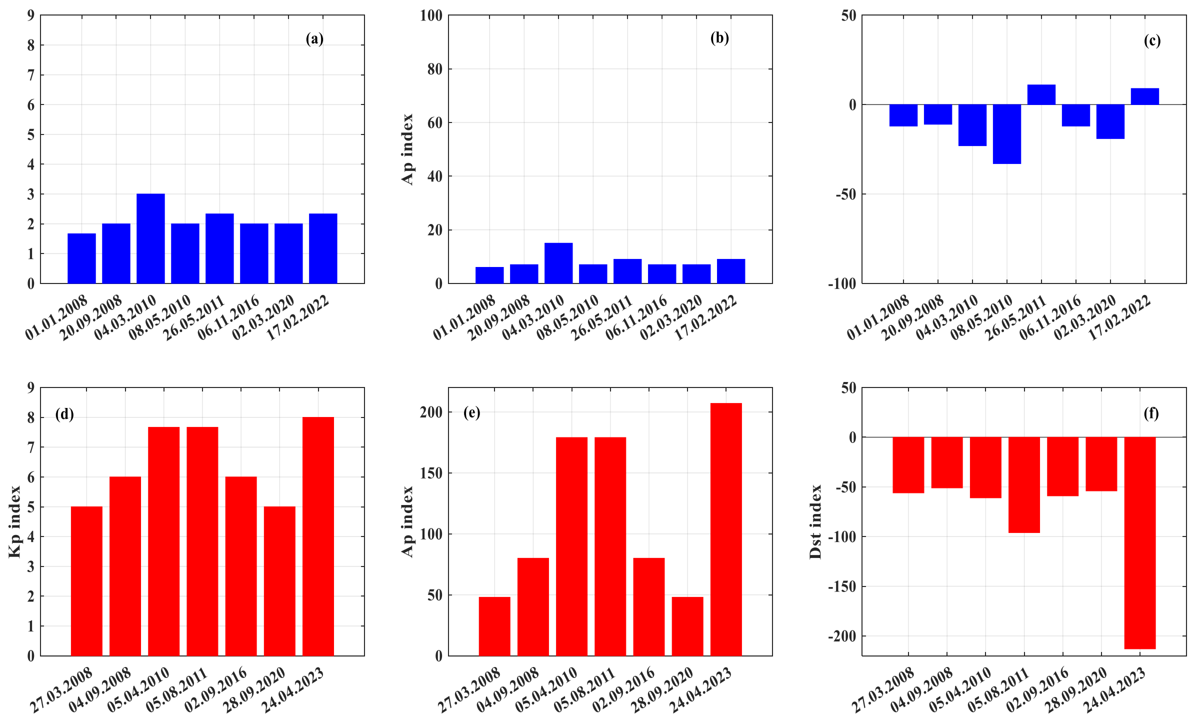

Fig. 3 Maximum values of the geomagnetic indices a) Kp indices, b) Ap indices and c) Dst indices for geomagnetically quiet days and d) Kp indices, e) Ap indices and e) Dst indices for geomagnetically disturbed days for both two groups of the study (GFZ, 1956; WDC, 1957)

The ionosphere shows relatively lower disturbance levels in periods before the major earthquakes listed in Table 1 compared to days with significant geomagnetic activity. Although the selected "quiet days" may have Kp values reaching up to 5.6 (classified as 'minor geomagnetic activity' according to NOAA's Space Weather Scale), these days were chosen as they represented the quiet geomagnetic conditions within the studied dataset. The highest recorded values in the dataset were 5.6 for Kp index, 67 for Ap index and -67 nT for Dst index.

This selection approach helped minimize geomagnetic influences, making it easier to identify ionospheric disturbances that might be associated with earthquake activity. During the period of the Türkiye earthquakes, the ionosphere was in much quieter conditions than during the period of the world earthquakes. Maximum values of Kp, Ap and Dst indices were 4, 27 and -32 nT on October 29, 2020, respevtively.

Fast Fourier Transform Implementation

Any periodic signal described in the time domain can be represented in the frequency domain using the Fourier Transform. For signals sampled at discrete intervals, the Discrete Fourier Transform (DFT) divides the signal into its constituent frequency components over time or space (Wang, 1984; Candan, et al., 2000; Sundararajan, 2001; Bagchi & Mitra, 2012; Olson, 2017). The Fast Fourier Transform (FFT), a computationally efficient algorithm for calculating the DFT, is employed in this study. Specifically, the IONOLAB-FFT algorithm is utilized to analyze ionospheric Total Electron Content (TEC) data. This approach has been selected for its ability to detect the main frequency components that comprise significant portions of the signal's spectrum, to identify the potential periodic variations in the TEC data and to isolate frequency signatures that might be associated with seismo-ionospheric phenomena.

The IONOLAB-TEC data computed for day d and station u using the transpose operator T, sample number n and total number of samples N can be defined as follows:

$$\boldsymbol{x}_{u;d}(n) = \left[x_{u;d}(1) \dots \dots x_{u;d}(n) \dots \dots x_{u;d}(N)\right]^T \quad (1)$$

The ionospheric Total Electron Content (TEC) data underwent a systematic filtering process to isolate potential disturbances from background variations. Initially, a sliding window median filter with a window length of 12.5 minutes was applied to the raw TEC data ($\boldsymbol{x}_{u;d}$) to remove short-term fluctuations and measurement noise. Subsequently, a second sliding window median filter with a considerably longer window length of 4.2 hours was employed to estimate the TEC trend structure, representing longer-term ionospheric behavior. To isolate potential disturbances, the difference vector, $\boldsymbol{D}_{f_{u;d}}$, is calculated between the first median filtered data and the second median filtered TEC. This difference effectively represents deviations from the background trend that might be associated with ionospheric perturbations. The temporal derivative of this difference vector, $\boldsymbol{D}_{u;d}$, is then computed using the following formula:

$$\boldsymbol{D}_{u;d} = \frac{d\left(\boldsymbol{D}_{f_{u;d}}\right)}{dt} \quad (2)$$

To further smooth this derivative data, we applied an additional sliding window median filter with a window length of 7.5 minutes to $\boldsymbol{D}_{u;d}$, yielding the smoothed derivative $\widetilde{\boldsymbol{D}}_{u;d}$. This step allowed to better characterize the temporal evolution and magnitude of the disturbances.

In this study, a systematic approach is established to determine the durations of ionospheric disturbances. First, the maximum value of the absolute derivative, $\left|D_{u;d}(n)\right|$, is computed across all data points within a given day. To identify significant disturbances while filtering out noise, a threshold is established at 1% of this maximum value. The index corresponding to the first value exceeding this threshold is designated as the starting point of the disturbance. This value is denoted as $p_{u;d}(1)$, which represents the first value of the new difference derivative, $\boldsymbol{D}_{p_{u;d}}$, as expressed in Equation (3):

$$\boldsymbol{D}_{p_{u;d}} = \left[p_{u;d}(1) \dots p_{u;d}(n_p) \dots p_{u;d}(N_p)\right]^T \quad (3)$$

where $p_{u;d}$ denotes the disturbance durations for station u and day d. The final value $p_{u;d}(N_p)$ of $\boldsymbol{D}_{p_{u;d}}$ is determined for those components where all absolute values fall below the established threshold, with $1 \leq n_p \leq N_p$. The parameter Np thus represents the total duration containing derivative values ($\boldsymbol{D}_{u;d}$) whose magnitude remains within 1% of the maximum absolute amplitude.

Frequency domain analysis

The smoothed derivative of the difference vector $\widetilde{\boldsymbol{D}}_{u;d}$ is then analyzed in the frequency domain using the Discrete Fourier Transform (DFT), represented by:

$$\boldsymbol{F}_{u;d}(k) = \sum_{n_f=0}^{N_f-1} \widetilde{D}_{u;d}(n_f) e^{-i2\pi k n_f/N_f} \quad (4)$$

where $F_{u;d}(k)$ represents the frequency components of $\widetilde{D}_{u;d}(n_f)$, N_f is the total number of data points and k represents the frequency index ($0 \leq k \leq N_f - 1$). For computational efficiency, the DFT is implemented using the Fast Fourier Transform (FFT) algorithm. Specifically, the IONOLAB-FFT algorithm is employed as described in previous literature (Arikan & Yarici, 2017; Karatay, 2020a; Karatay, 2020b) to extract key frequency components associated with potential ionospheric disturbances.

The IONOLAB-FFT algorithm adds a loop to the n_L loop counter to retrieve the frequency components that correspond to the maximum power in order to identify the most important frequency components of the smoothed derivative spectrum. First, $n_L = 1$ is shown to have the highest magnitude component of the data in the frequency domain as $a_{u;d}(1) = max(|\boldsymbol{F}_{u;d}(k)|)$. Finally, the main lobe is approximated in order to determine the inflection point associated with the largest magnitude.

Extraction of key frequency components

The IONOLAB-FFT algorithm identifies dominant spectral components through an iterative process. The technique appends a loop to the main processing routine, enabling the identification of the inflection point associated with the maximum amplitude. This inflection point corresponds to the major lobe in the frequency spectrum.

The components of the estimated major lobe can be characterized as sinusoidal functions. The sum of these sine functions determines the percentage contribution to the normalized total difference with derivative data. The extraction of the estimated major lobe from the spectrum in the frequency domain is performed using Equation (4), leading to:

$$\widetilde{\boldsymbol{D}}_{u;d}(n;1) \approx \sum_{n_s=1}^{N_s} A_{n_s} \sin\left(2\pi f_{n_s} t + \Phi_{n_s}\right) \quad (5)$$

where A_{n_s} represents the amplitude, f_{n_s} is main frequency in the main lobe and Φ_{n_s} is the phase of each identified spectral component with N_s being the total number of extracted components. Using Equation (5), the frequencies are calculated corresponding to the highest amplitudes, which represent the most significant periodic variations in the ionospheric TEC data.

The percentage of the normalized total difference using derivative data is determined by adding these sine functions together as follows:

$$e_{u;d}(1) = \frac{|\boldsymbol{D}_{u;d} - \widetilde{\boldsymbol{D}}_{u;d}(1)|_2}{|\boldsymbol{D}_{u;d}|_2} x100 \tag{6}$$

At this step, if $e_{u;d}(1) \geq 40\%$, the estimated main lobe is extracted from spectrum in the frequency domain (Arikan & Yarici, 2017; Karatay, 2020a; Karatay, 2020b). The loop then continues until $e_{u;d}(1) < 40\%$ when the algorithm returns to $a_{u;d}(1) = max\left(\left|\boldsymbol{F}_{u;d}(k)\right|\right)$. The most important frequencies are obtained as follows:

$$\boldsymbol{f}_{u;d} = \left[f_{u;d}(n) \ldots\ldots f_{u;d}(n_L) \ldots\ldots f_{u;d}(N_L)\right]^T \tag{7}$$

The IONOLAB-FFT approach is used in the following analysis to examine TEC data estimated from several IGS stations located in various seismic areas across the world. The analysis is carried out for two different time periods: during geomagnetically quiet days and during the periods surrounding thirteen significant earthquake events. Comparing the frequency components observed during seismically active periods with those observed during quiet reference periods provides opportunity for the identification of possible seismo-ionospheric precursors. To ensure the robustness of our findings, statistical significance has been assessed for all correlation coefficients reported in this study. Correlation values exceeding 0.7 have been found to be statistically significant at $p < 0.01$, while those between 0.5-0.7 have been significant at $p < 0.05$. For frequency-duration relationships, the power law fits have been validated using both coefficient of determination (R^2) values and residual analysis to confirm that the observed relationships have not been the result of random variations. The consistently high correlation coefficients observed across different earthquake magnitudes and geographic regions (ranging from 0.81 to 0.97 for high-magnitude events) provide strong statistical evidence for the reliability of the identified seismo-ionospheric patterns.

Experimental Probability Density Function (EPDF) Generation

Following the extraction of dominant frequency components using the IONOLAB-FFT algorithm, Experimental Probability Density Functions (EPDFs) are constructed to characterize the statistical distribution of frequency values across all stations and time periods. The EPDF generation process involves several systematic steps designed to enable comparative analysis between different seismic and geomagnetic conditions.

The frequency values obtained from Equation (7) for all stations within each earthquake network are pooled together to create comprehensive datasets for each analyzed day. For a given day d and station network consisting of M stations, the combined frequency dataset $\boldsymbol{F}_{combined;d}$ is formed as:

$$\boldsymbol{F}_{combined,d} = \left[\boldsymbol{f}_{1;d}, \boldsymbol{f}_{2;d}, \ldots\ldots \boldsymbol{f}_{M;d}\right] \tag{8}$$

The frequency range of interest (0 to 1.4 mHz for world earthquakes, 0 to 3.5 mHz for Türkiye earthquakes) is divided into equal-width bins with a resolution of 0.05 mHz. This bin width was selected to provide sufficient statistical resolution while maintaining adequate sample sizes within each bin for reliable probability estimation. For each bin i with center frequency f_i, the number of frequency values n_i falling within the bin boundaries $[f_i - \Delta f/2, f_i + \Delta f/2,]$ is counted, where $\Delta f = 0.05$ mHz represents the bin width. The histogram H_i for each bin is computed as:

$$H_i = n_i / N_{total} \tag{9}$$

where N_total is the total number of frequency values in the combined dataset. To convert the histogram into a proper probability density function, area normalization is applied:

$$EPDF_i = H_i / \Delta f \tag{10}$$

This normalization ensures that the integral of the EPDF over the entire frequency range equals unity, satisfying the fundamental requirement of Probability Density Functions. The resulting EPDF values represent the probability density per unit frequency (mHz^{-1}), enabling direct comparison between different time periods and earthquake scenarios regardless of the total number of observations.

Data Processing and Visualization Examples

To demonstrate the practical implementation and transparency of the IONOLAB-FFT methodology, this section presents detailed visualization examples of the complete processing pipeline. The examples illustrate the step-by-step transformation of raw GNSS-TEC measurements into frequency-duration statistics, providing clear insight into how each mathematical operation (Equations 1-10) contributes to the final seismo-ionospheric analysis. Using representative data from the STK2 station during the pre-Tohoku earthquake period, the systematic filtering, derivative calculation, FFT analysis and statistical processing steps are demonstrated in order to enable the detection of spectral tracks in ionospheric Total Electron Content variations. These visualizations serve both as validation of the methodology and as a practical guide for researchers implementing similar seismo-ionospheric coupling studies.

Fig. 4 shows the IONOLAB-FFT processing pipeline flowchart for seismo-ionospheric coupling analysis. The diagram illustrates the systematic transformation of raw GNSS-TEC data through ten sequential steps (Equations 1-10): data input, dual median filtering, temporal derivative calculation, smoothing, duration analysis, Fast Fourier Transform, main lobe extraction, error assessment, iterative processing decision, frequency extraction, multi-station data combination, histogram generation, and experimental probability density function (EPDF) calculation. The flowchart demonstrates the complete methodology for detecting spectral tracks in ionospheric Total Electron Content variations preceding earthquake events.

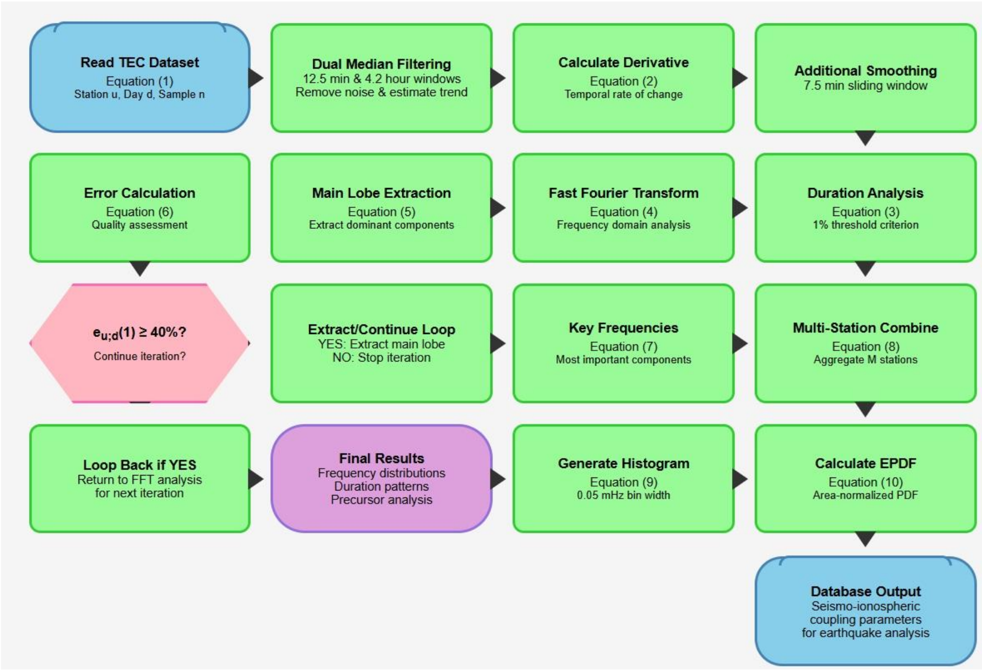

Fig. 4 IONOLAB-FFT algorithm flowchart showing the complete processing pipeline from raw TEC data to seismo-ionospheric precursor analysis. The methodology encompasses ten sequential steps (Equations 1-10) including filtering, frequency domain analysis, iterative processing, and statistical evaluation for earthquake prediction through ionospheric monitoring

Fig. 5 shows the complete IONOLAB-FFT processing pipeline demonstrating the step-by-step mathematical transformation from raw GNSS-TEC measurements to frequency-duration statistics. Single-day analysis using data from STK2 station on March 08, 2011, representing 3 days before the Tohoku earthquake (Mw 9.0, March 11, 2011). Each subplot (a–l) corresponds directly to the mathematical equations (1–10) detailed in Section 3, providing transparent visualization of the complete processing chain.

Fig. 5 (a) shows raw TEC time series $\boldsymbol{x}_{u;d}$ showing typical diurnal ionospheric variation with values ranging from 9.12 to 27.33 TECU; Fig. 5 (b) and (c) show dual median filtering process (12.5-minute and 4.2-hour windows) for noise reduction and background trend estimation and temporal derivative calculation $\boldsymbol{D}_{u;d}$ highlighting rapid TEC variations and potential ionospheric disturbances. Fig. 5 (d) and (e) show smoothed derivative $\widetilde{\boldsymbol{D}}_{u;d}$ using 7.5-minute sliding window median filter to reduce high-frequency noise and duration vector calculation using 1% threshold criterion for disturbance identification, showing periods exceeding the threshold. Fig 5 (f) and (g) show duration analysis summary displaying total disturbance time (above threshold) within the 24-hour period and FFT magnitude spectrum $\boldsymbol{F}_{u;d}(k)$ revealing dominant frequency components in the 0–2 mHz range. Fig 5 (h) and (I) show IONOLAB-FFT main lobe identification and secondary peak detection following Equation (5) and extracted frequency components $\boldsymbol{f}_{u;d}$ representing significant spectral features with normalized amplitudes. Fig. 5 (j) and (k) show combined frequency dataset simulation demonstrating multi-station data aggregation for statistical analysis and histogram generation and EPDF normalization process following Equations (9–10), showing both normalized count H_i and probability density function. Finally, Fig. 5 (l) shows frequency-duration relationship analysis demonstrating the inverse correlation characteristic of seismo-ionospheric coupling phenomena.

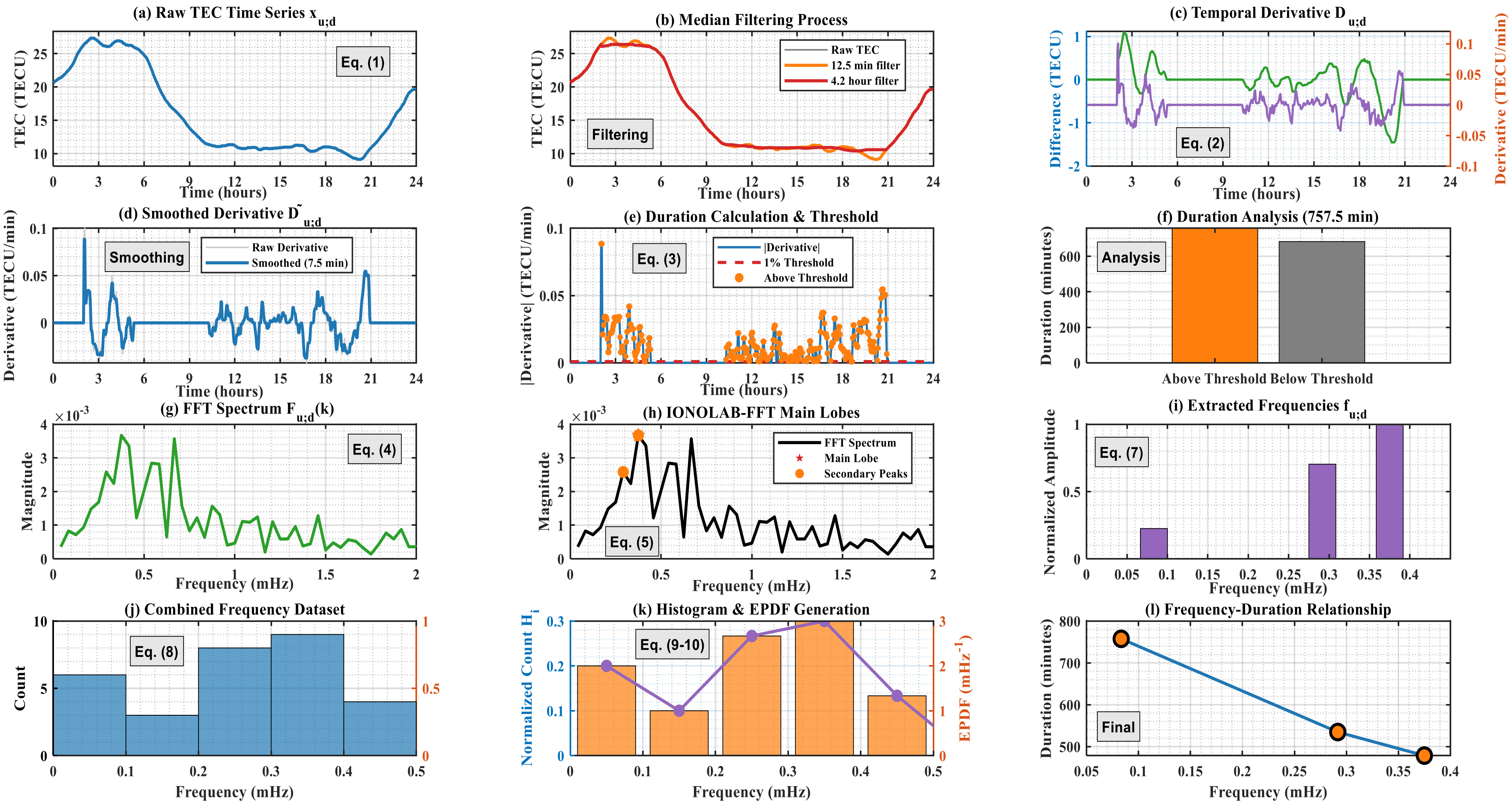

Fig. 5 (a) Raw TEC time series $\boldsymbol{x}_{u;d}$; (b) Dual median filtering process (12.5-minute and 4.2-hour windows); (c) Temporal derivative calculation $\boldsymbol{D}_{u;d}$;(d) Smoothed derivative $\widetilde{\boldsymbol{D}}_{u;d}$; (e) Duration vector calculation and threshold; (f) Duration analysis; (g) FFT magnitude spectrum $\boldsymbol{F}_{u;d}(k)$; (h) IONOLAB-FFT main lobes; (i) Extracted frequency components $\boldsymbol{f}_{u;d}$; (j) Combined frequency dataset; (k) Histogram generation and EPDF normalization; (l) Frequency-duration relationship

The peak EPDF value, dominant frequency (frequency corresponding to maximum EPDF), and bandwidth (frequency range containing 80% of the total probability) are extracted as key parameters for quantitative analysis and correlation studies presented in the Analysis and Discussion Section.

Analysis and Discussion

This study investigates the presence of geomagnetic and seismic disturbance precursor signals in the ionosphere by applying the IONOLAB-FFT algorithm to IONOLAB-TEC data. The data from multiple GPS stations is analyzed (illustrated in Figures 1 and 2) during known periods of seismic and geomagnetic activity. The analysis focuses on thirteen major earthquakes with magnitudes ranging from Mw 5.6 to 9.0, as detailed in Table 3. For each earthquake, both the day of the event and the preceding five days are examined to identify potential seismic precursors. For comparison and to differentiate between seismic and geomagnetic disturbances, the algorithm is also applied to periods of geomagnetic quiescence and heightened activity, selecting days with the highest Kp index values for the respective years. In contrast to measurement artifacts or known periodic variations, this ensures that any detected frequency components would reflect significant ionospheric behavior.

The IONOLAB-FFT algorithm is applied to daily IONOLAB-TEC values across all selected stations and time periods. Experimental Probability Density Functions (EPDFs) are then generated by organizing the frequency values into area-normalized bins. Results are presented in two distinct categories: world earthquakes (nine events) and earthquakes specific to Türkiye (four events). This approach enables a comprehensive assessment of pre-seismic spectral variations in the ionosphere preceding significant seismic events. The goal of this frequency domain analysis is to show subtle periodic spectral tracks that may be lost in time-domain representations and to describe the dominant periodic patterns in ionospheric TEC variations.

World earthquakes

In the first group of the study, the IONOLAB-FFT algorithm is applied to IONOLAB-TEC data estimated for nine earthquake periods given in Table 1 and Fig. 1 and a geomagnetic disturbance and a quiet day for the corresponding years of these earthquakes. Experimental Probability Density Functions (EPDFs) are obtained by organizing the frequency values into area-normalized bins for pre-seismic, co-seismic, disturbed and quiet periods given in Table 3 for each station given in Table 1 and Fig. 1. The durations are also computed for four all periods for all stations.

Fig. 6 presents a comprehensive visualization of ionospheric behavior during both geomagnetically quiet and disturbed periods across multiple stations for the nine earthquakes occurred in the different locations in the world (E1-E9) analyzed in this study. The figure is organized into four main components that reveal distinct patterns of ionospheric variations. The top two rows ((a1)-(a8) and (b1)-(b8)) display Experimental Probability Density Functions (EPDFs) of frequency values ranging from 0 to 1.4 mHz. The bottom two rows ((c1)-(c8) and (d1)-(d8)) illustrate the durations of these fluctuations across various stations.

During seismically quiet periods, frequency distributions across all station networks show relatively uniform patterns with gradual declining trends from lower to higher frequencies. Most stations exhibit peak EPDF values in the 0.2-0.4 mHz range, with frequency distributions predominantly following a right-skewed pattern. This consistency during quiet periods establishes an important baseline for comparison with both disturbed periods and pre-earthquake conditions. For stations monitoring the Japanese earthquakes (Fig. 6 (a1), (a5)), the quiet period frequency distribution maintains the highest consistency, with PDF values gradually decreasing from approximately 0.25 at 0.2 mHz to 0.05 at 1.4 mHz. The Chilean station network (Fig. 6 (a2)) shows slightly higher variability while maintaining a similar declining trend. During seismically disturbed periods, frequency distributions show more pronounced peaks in the low-frequency range (0.2-0.4 mHz) compared to quiet periods. The PEDF values at low frequencies increase by approximately 15-30% across most station networks, indicating a significant shift toward lower frequency dominance during disturbed periods. The most substantial shifts are observed in stations monitoring the highest-magnitude earthquakes, particularly those in Japan (Fig. 6 (b1), (b5)) and Chile (Fig. 6 (b2)), where low-frequency EPDF values reach up to 0.3 mHz, compared to approximately 0.25 mHz during quiet periods. This pattern suggests a correlation between disturbance intensity and the magnitude of frequency distribution shifts.

Duration measurements during quiet periods show considerable variability between stations within each network. The Japanese station network (Fig. 6 (c1), (c5)) displays durations ranging from approximately 300 to 700 minutes, with several stations consistently registering higher values. The Chilean network (Fig. 6 (c2)) shows more uniform duration distribution across stations, ranging from 400 to 600 minutes. The Chinese station network (Fig. 6 (c3), (c7)) exhibits the greatest station-to-station variability during quiet periods, with some stations recording durations above 800 minutes while others remain below 300 minutes. This variability may reflect regional geological differences affecting background signal characteristics. During disturbed periods, duration measurements show both increased magnitudes and greater station-to-station variability compared to quiet periods. Several stations across all networks record duration increases of 20-30% during disturbed periods, with maximum values exceeding 800 minutes for multiple stations. The Japanese network (Fig. 6 (d1), (d5)) shows the most consistent increase in durations across all stations during disturbances. The Chilean network (Fig. 6 (d2)) exhibits more selective increases, with some stations showing minimal change while others display substantial duration increases. The Mexican station network (Fig. 6 (d4)) shows the most dramatic relative increase in durations during disturbed periods compared to quiet conditions. This increased variability during geomagnetically disturbed periods suggests that geomagnetic activity may induce irregular and station-dependent ionospheric responses. This accurately reflects that the disturbed periods shown in Fig. 6 may relate to geomagnetic disturbances (high Kp index days).

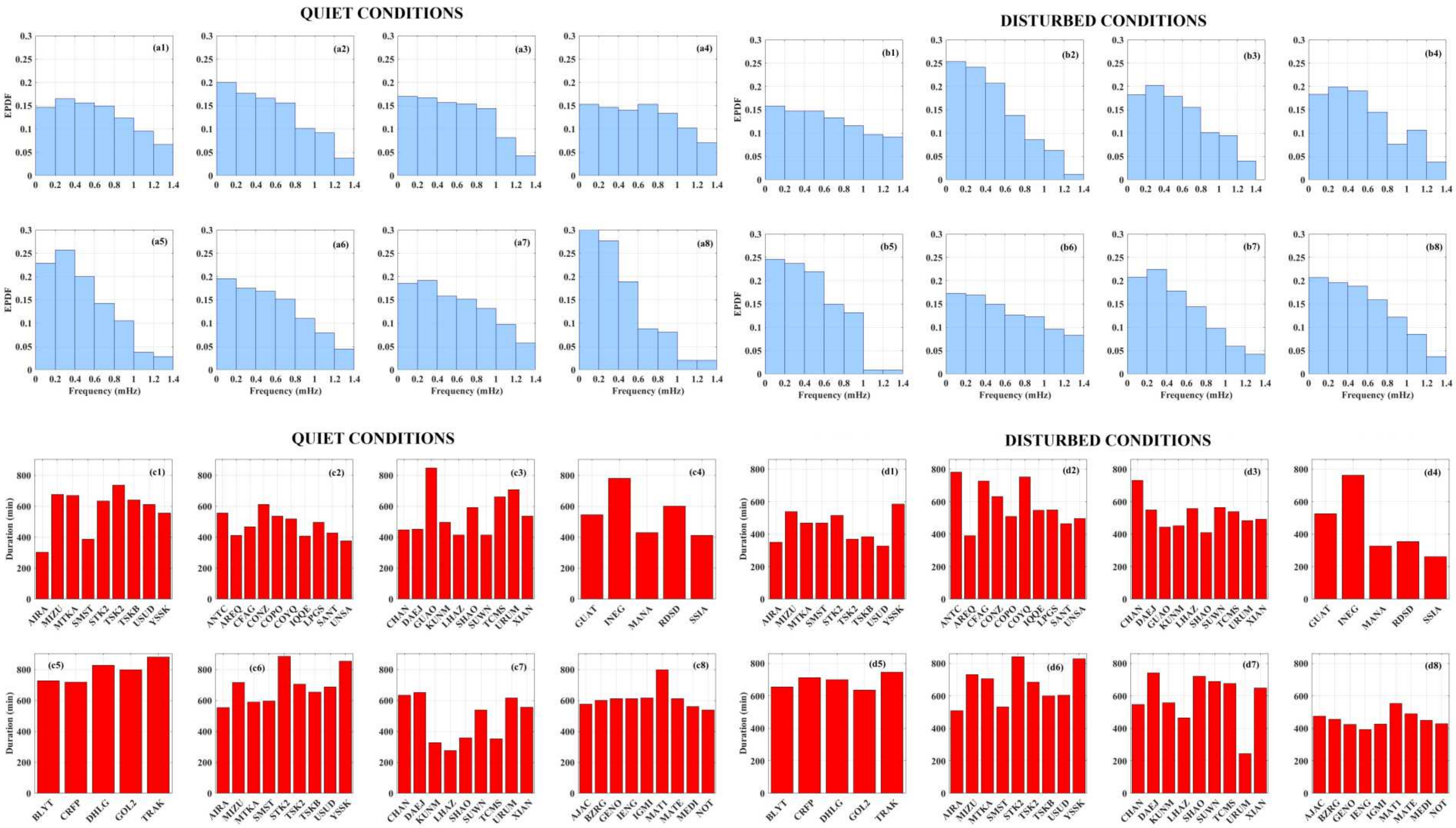

Fig. 6 (a1)-(a8) quiet period EPDFs of the frequency values for all stations used in E1-E9 earthquakes, (b1)-(b8) disturbed period EPDFs of the frequency values for all stations used in E1-E9 earthquakes, (c1)-(c8) quiet period durations for all stations used in E1-E9 earthquakes, (d1)-(28) disturbed period durations for all stations used in E1-E9 earthquakes

Figures 7-14 show the Experimental Probability Density Functions (EPDF) of the frequency values and the durations values on the day of E1-E9 earthquakes with magnitudes ranging from 5.6 to 9.0 on the Richter scale occurring in various geographic locations including Japan, Chile, China, Mexico, USA, and Italy, one day before, two days before, three days before, four days before and five days before the each earthquake for all stations used in the related earthquake.

Fig. 7 illustrates significant transformations in frequency distribution patterns over the five days preceding this mega-thrust event E1 (Tohoku, Japan Mw 9.0). On the earthquake day (a1), frequency values display a bimodal distribution with distinct peaks at approximately 0.2 mHz and 0.4 mHz with the higher frequency peak showing greater amplitude. A systematic evolution is observed from 5 days prior (a6) to the event day with the secondary peak gradually becoming more pronounced. Duration analysis (b1)-(b6) indicates a significant increase in high-frequency events from ~0.33 minutes 5 days prior to ~1.0-1.3 minutes on the earthquake day. The most dramatic shift occurs between 2 days prior (a3) and the day before (a2), where the amplitude ratio between the two frequency peaks inverts.

Fig. 8 demonstrates comparable but distinct precursory patterns for this high-magnitude event E2 (Maule, Chile Mw 8.8). The frequency distribution 5 days prior (a6) shows a relatively uniform distribution centered around 0.25 mHz. A progressive development of a bimodal pattern emerges from day 4 (a5) through day 1 (a2). On the earthquake day (a1), the frequency distribution exhibits a pronounced peak at approximately 0.3 mHz with a secondary peak at 0.5 mHz. Duration measurements (b1)-(b6) show a significant increase in longer-duration events (~0.67-1.0 minutes) on the earthquake day compared to the predominantly short durations (~0.17-0.33 minutes) observed 5 days prior.

As depicted in Fig. 9, this high-magnitude continental event E3 (Wenchuan, China Mw 7.9) is presented distinctive signal characteristics. The frequency distribution 5 days prior (a6) shows a relatively normal distribution centered at approximately 0.3 mHz. Days 4-2 prior (a5)-(a3) show a gradual development of a secondary peak at approximately 0.5 mHz. The day before the earthquake (a2) shows a marked shift toward a bimodal distribution with nearly equal amplitudes at 0.2 mHz and 0.4 mHz. On the earthquake day (a1), the distribution shifts predominantly to higher frequencies (0.4-0.5 mHz). Duration analysis (b1)-(b6) shows a clear transition from predominantly short-duration events (~0.25-0.42 minutes) 5 days prior to a broader distribution including more long-duration events (~0.67-1.0 minutes) on the earthquake day.

Fig. 10 reveals more subtle precursory signals for this intermediate-magnitude event E4 (Oaxaca, Mexico Mw 7.4). A relatively stable frequency distribution centers at approximately 0.25 mHz from days 5-3 prior ((a6)-(a4)). A noticeable shift begins 2 days prior (a3) with the emergence of a secondary peak at approximately 0.4 mHz. On the earthquake day (a1), a distinct bimodal distribution is observed with peaks at approximately 0.2 mHz and 0.45 mHz. Duration measurements (b1)-(b6) show a particularly pronounced shift from predominantly short durations (~0.17-0.33 minutes) 5 days prior to a significant increase in longer-duration events (~0.83-1.17 minutes) on the earthquake day.

As shown in Fig. 11, E5 earthquake (California, USA Mw 7.2) is exhibited frequency distributions (Fig. 11 (a1)-(a6)) that maintains relatively stable patterns until approximately three days before the earthquake, when a noticeable shift toward lower frequencies becomes evident. A relatively consistent unimodal distribution centers at approximately 0.3 mHz from days 5-3 prior ((a6)-(a4)). Two days prior (a3), the emergence of a secondary peak is observed at approximately 0.5 mHz. One day prior (a2), a clear bimodal distribution is observed with nearly equal amplitudes. On the earthquake day (a1), a predominance of higher frequency components emerge around 0.4-0.5 mHz. Duration analysis (b1)-(b6) shows a moderate increase in longer-duration events (~0.5-0.83 minutes) on the earthquake day compared to primarily short durations (~0.25-0.42 minutes) observed 5 days prior.

Fig. 12 demonstrates that for the lower-magnitude event E6 (Iwate, Japan Mw 6.9), precursory signal changes are considerably less pronounced. Initially stable frequency distribution centers around 0.25 mHz from days 5-3 prior ((a6)-(a4)). A subtle emergence of a secondary peak at approximately 0.4 mHz begins 2 days prior (a3). On the earthquake day (a1), a more pronounced bimodal distribution is observed with peaks at approximately 0.2 mHz and 0.45 mHz. Duration analysis (b1)-(b6) demonstrates a gradual increase in the proportion of longer-duration events (~0.5-0.75 minutes) approaching the earthquake day.

Similar to E6, Fig. 13 reveals subtle signal alterations for E7 earthquake (Yushu, China Mw 6.9). Frequency EPDFs (Fig. 13 (a1)-(a6)) maintain relatively consistent patterns until approximately 48 hours before the earthquake, when a minor shift toward lower frequencies is observed. A predominantly unimodal distribution centers at approximately 0.25 mHz from days 5-2 prior ((a6)-(a3)). The day before the earthquake (a2), a noticeable broadening of the distribution is observed with enhanced higher-frequency components. On the earthquake day (a1), a bimodal distribution emerges with peaks at approximately 0.2 mHz and 0.4 mHz. Duration analysis (b1)-(b6) shows a less dramatic but still perceptible increase in longer-duration events (~0.42-0.67 minutes) on the earthquake day compared to prior days.

Fig. 14 presents the lowest-magnitude dual Italy earthquakes E8 and E9 (Norcia, Italy Mw 6.2 and 5.6) in the study, characterized by the most subtle signal alterations. A relatively stable frequency distribution centers around 0.3 mHz from days 5-3 prior ((a6)-(a4)). Beginning 2 days prior (a3), a gradual development of a bimodal pattern is observed. On the earthquake day (a1), a clear bimodal distribution emerges with peaks at approximately 0.25 mHz and 0.45 mHz. Duration analysis (b1)-(b6) shows a modest increase in longer-duration events (~0.5-0.67 minutes) on the earthquake day compared to predominantly shorter durations (~0.25-0.42 minutes) 5 days prior.

Our analysis reveals distinct patterns when comparing GNSS signal characteristics during earthquake periods (Fig. 7-14) with those during geomagnetically quiet and disturbed periods (Fig. 6). The frequency distributions and durations exhibit notable variations that correlate with both earthquake magnitude and temporal proximity to seismic events. Geomagnetically quiet periods (Fig. 6, (a1)-(a8)) demonstrate relatively concentrated frequency distributions with well-defined, narrow peaks in the mHz range. In contrast, geomagnetically disturbed periods (Fig. 6, (b1)-(b8)) present broader, more dispersed frequency distributions across the spectrum. This dispersion pattern bears striking similarities to the frequency distributions observed in the days preceding major earthquakes, particularly for events with magnitudes exceeding 8.0 on the Richter scale.

Examination of the temporal progression in Fig. 7-14 indicates a systematic evolution of frequency distributions as seismic events approach. The Tohoku, Japan earthquake (Mw 9.0, Fig. 7) exhibits the most pronounced transformation with frequency distributions gradually shifting from concentrated patterns similar to geomagnetically quiet periods to more dispersed distributions resembling geomagnetically disturbed conditions. This transformation becomes increasingly evident approximately 3-4 days before the seismic event, suggesting potential precursory signals detectable through GNSS frequency analysis. Duration patterns further substantiate these observations. During geomagnetically quiet periods (Fig. 6, (c1)-(c8)), durations remain relatively short and consistent. Conversely, disturbed periods (Fig. 6, (d1)-(d8)) display extended durations with greater variability. Our findings demonstrate that as earthquakes approach, duration patterns progressively resemble those of geomagnetically disturbed periods, with this effect proportional to earthquake magnitude. The Maule, Chile earthquake (Mw 8.8, Fig. 8) shows significant duration pattern changes beginning 2-3 days before the event, while the Wenchuan, China earthquake (Mw 7.9, Fig. 9) displays moderate but detectable changes approximately 2 days prior.

A clear magnitude-dependent relationship emerges across the dataset. Major earthquakes ($Mw \geq$ 8.0) consistently demonstrate the most dramatic alterations in both frequency and duration patterns with changes detectable up to 5 days before the seismic event. Strong earthquakes (Mw 7.0-7.9), represented by the Oaxaca, Mexico (Mw 7.4, Fig. 10) and California, USA (Mw 7.2, Fig. 11) events, exhibit moderate changes that become apparent 1-2 days before the earthquake. Moderate earthquakes (Mw 6.0-6.9), such as the Iwate, Japan (Mw 6.9, Fig. 12), Yushu, China (Mw 6.9, Fig. 13) and Norcia, Italy (Mw 6.2 and 5.6, Fig. 14) events, display subtler but still discernible pattern shifts. The observed correlation between GNSS signal characteristics and seismic activity suggests that GNSS frequency and duration monitoring could potentially serve as an early indicator of impending earthquakes. Particularly noteworthy is how the transformation from patterns resembling geomagnetically quiet conditions to those resembling disturbed conditions appears to precede seismic events. This transformation is most pronounced for high-magnitude earthquakes, where changes in frequency distributions and durations become increasingly apparent as the earthquake approaches with significant alterations typically manifesting 1-3 days before the event.

One of the most significant findings of our study is the remarkable similarity between GNSS signal patterns during pre-earthquake periods and those observed during geomagnetically disturbed conditions unrelated to seismic activity. As earthquakes approach, the frequency distributions progressively transform from patterns resembling geomagnetically quiet periods to those characteristic of disturbed periods. This transformation provides a potential mechanism for distinguishing genuine earthquake precursors from other sources of signal disturbance. The process from narrow, concentrated frequency distributions to broader, more dispersed distributions appears to be a consistent harbinger of impending seismic activity across all magnitude ranges. However, the temporal window during which this transformation occurs varies considerably with earthquake magnitude, from several days for major events to less than a day for moderate ones.

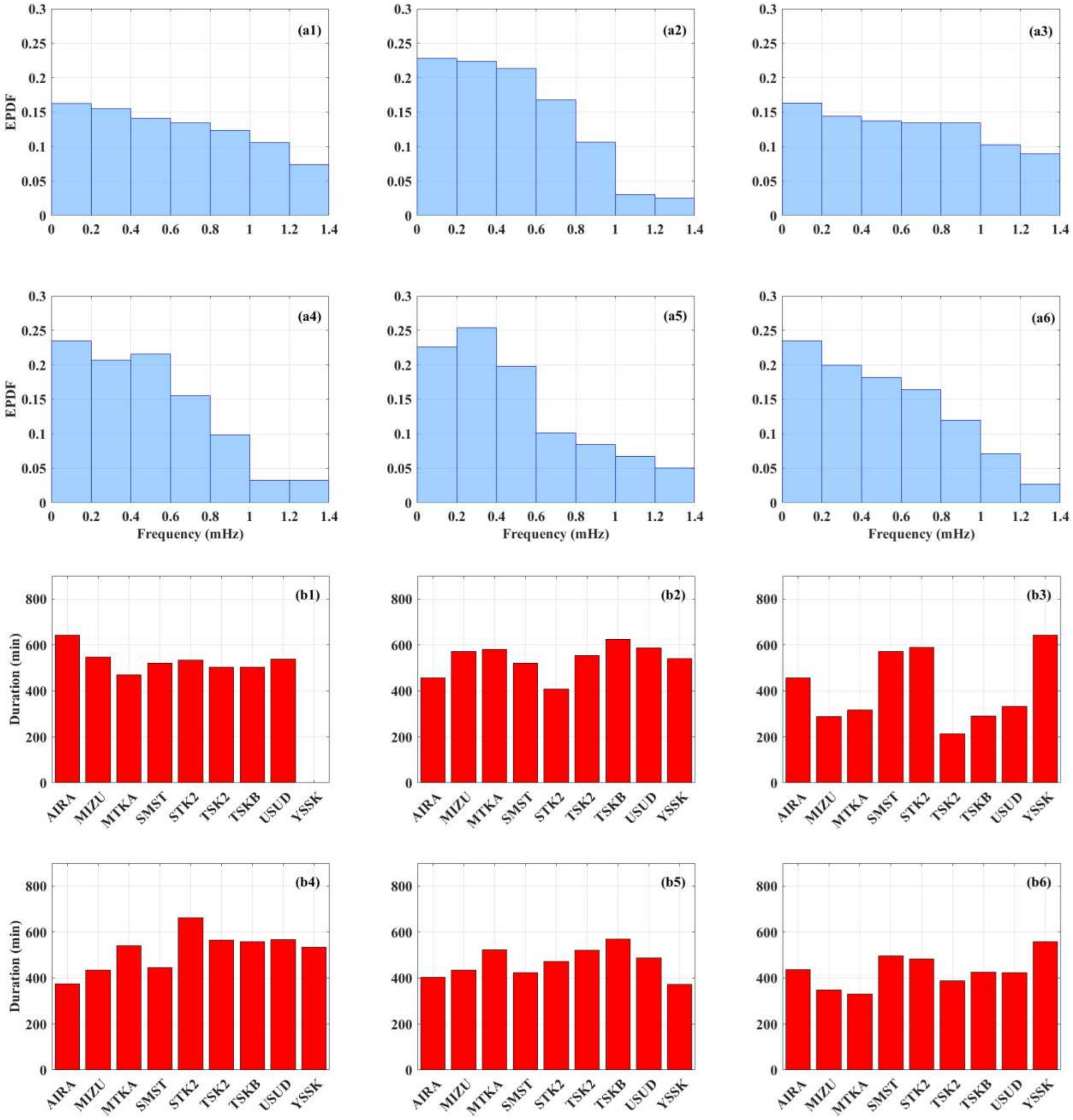

Fig. 7 (a1)-(a6) earthquake period EPDFs of the frequency values and (b1)-(b6) earthquake period durations on the day of the E1 earthquake (Mw 9.0), one day before the, two days before, three days before, four days before and five days before the E1 earthquake (Mw 9.0) for all stations

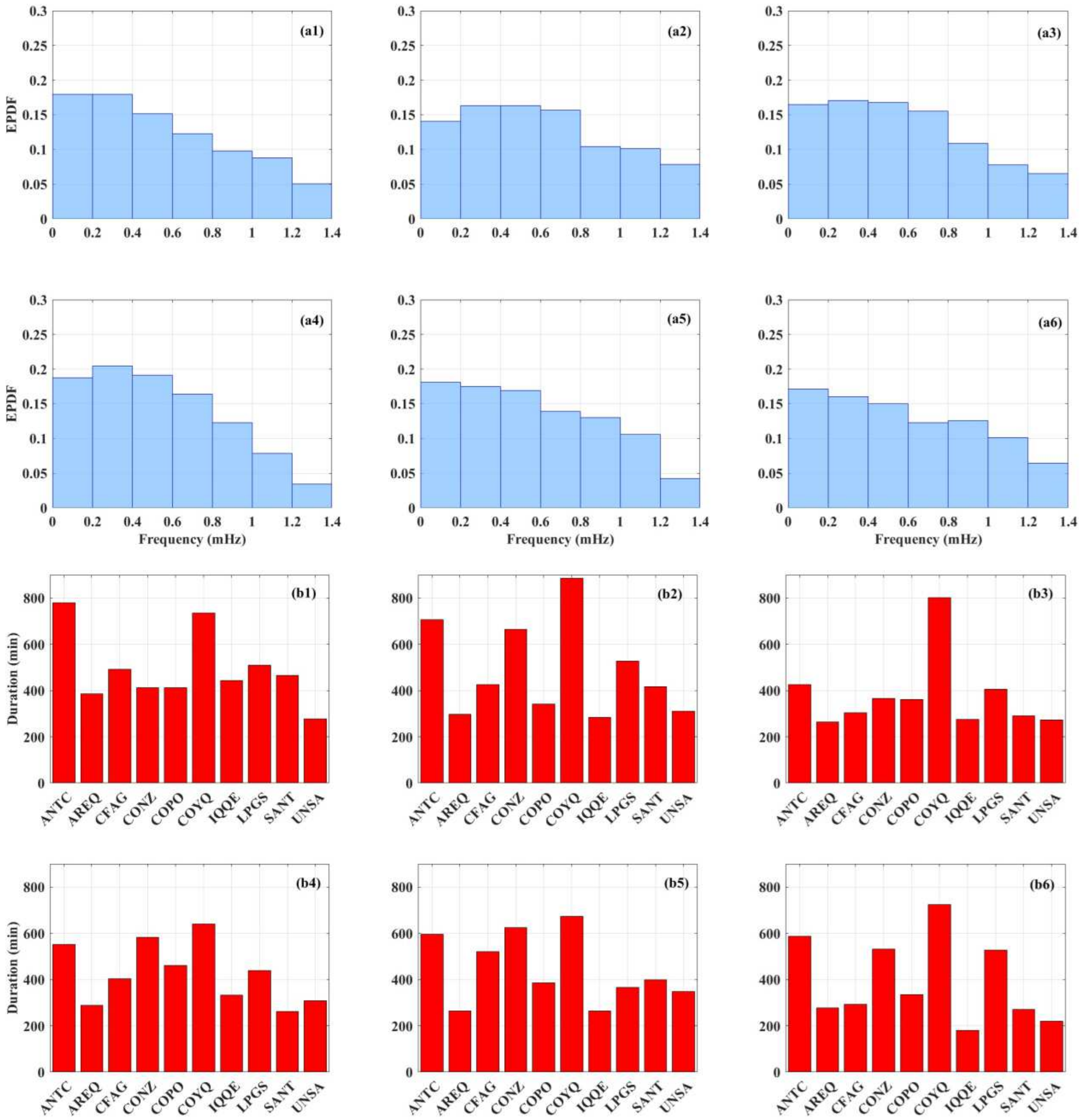

Fig. 8 (a1)-(a6) earthquake period EPDFs of the frequency values and (b1)-(b6) earthquake period durations on the day of the E2 earthquake (Mw 8.8), one day before the, two days before, three days before, four days before and five days before the E2 earthquake (Mw 8.8) for all stations

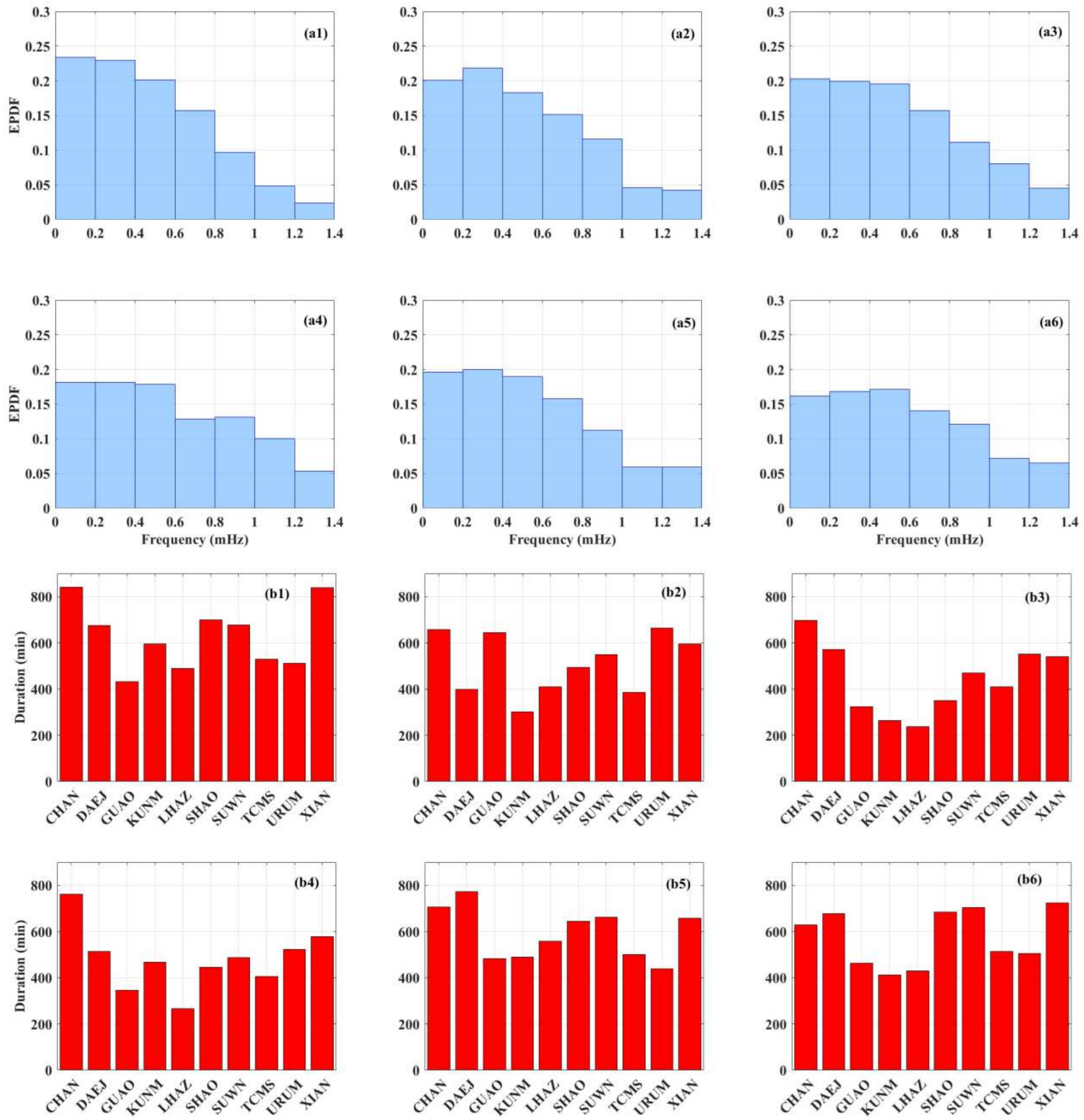

Fig. 9 (a1)-(a6) earthquake period EPDFs of the frequency values and (b1)-(b6) earthquake period durations on the day of the E3 earthquake (Mw 7.9), one day before the, two days before, three days before, four days before and five days before the E3 earthquake (Mw 7.9) for all stations

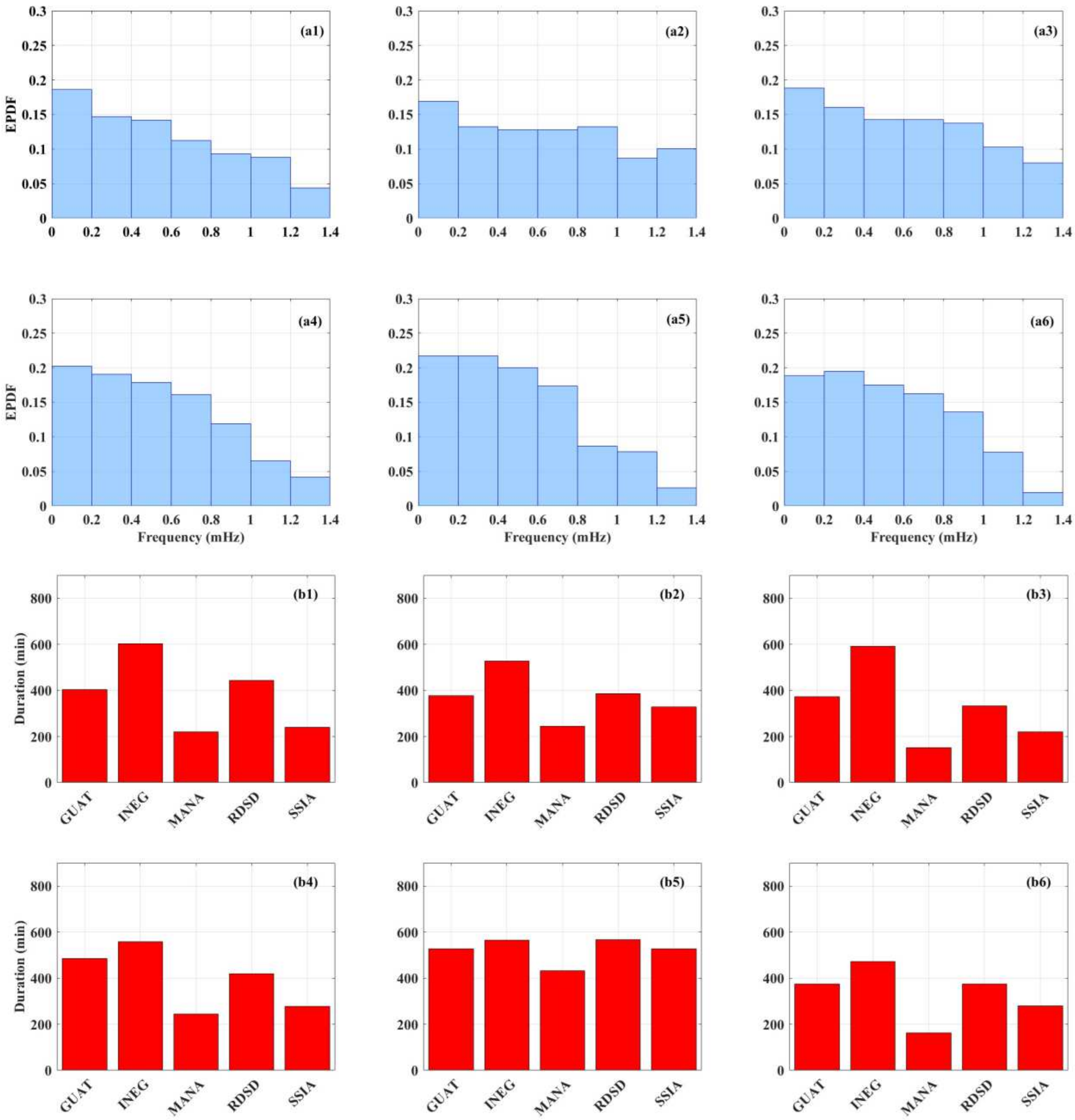

Fig. 10 (a1)-(a6) earthquake period EPDFs of the frequency values and (b1)-(b6) earthquake period durations on the day of the E4 earthquake (Mw 7.4), one day before the, two days before, three days before, four days before and five days before the E4 earthquake (Mw 7.4) for all stations

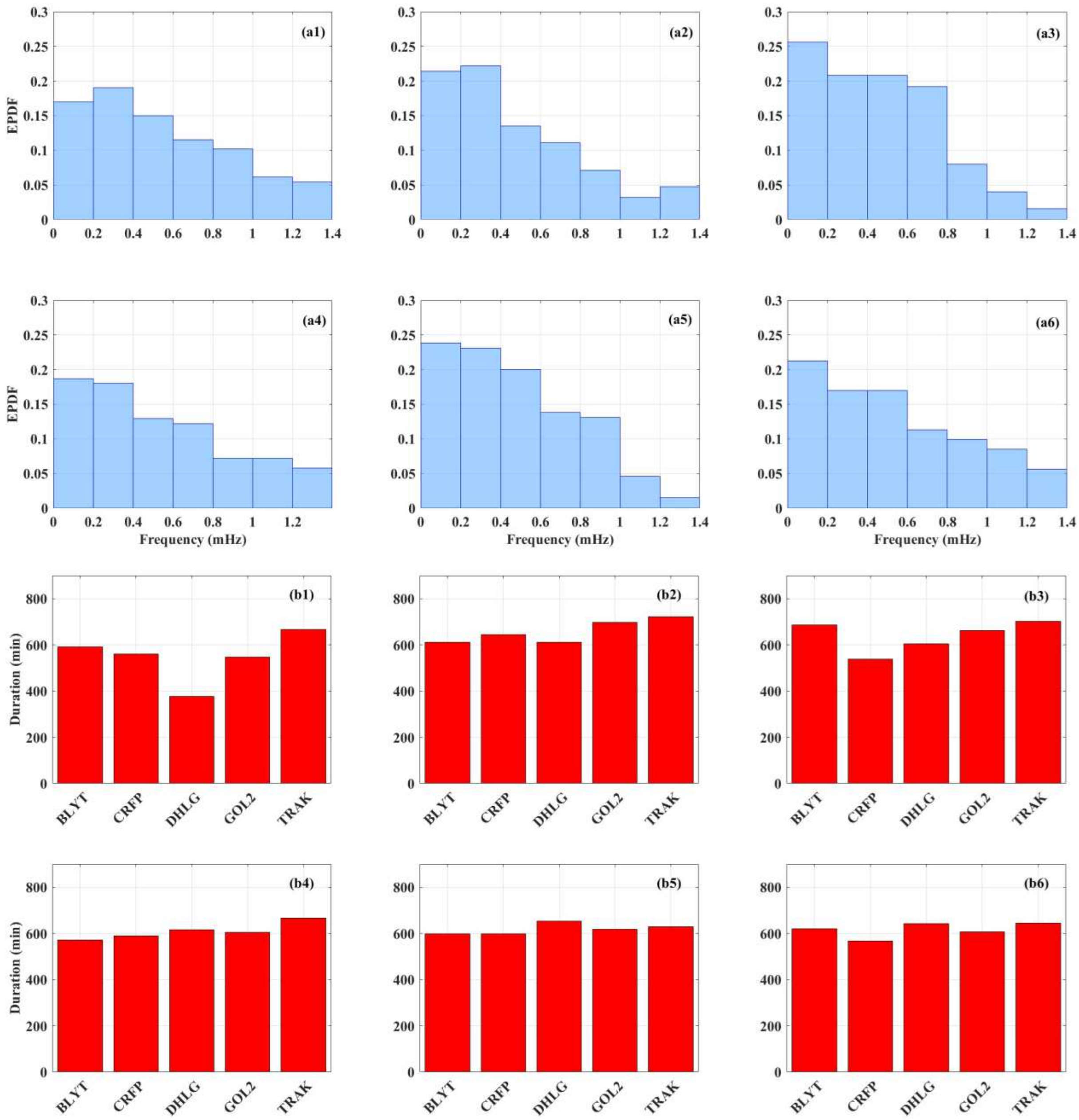

Fig. 11 (a1)-(a6) earthquake period EPDFs of the frequency values and (b1)-(b6) earthquake period durations on the day of the E5 earthquake (Mw 7.2), one day before the, two days before, three days before, four days before and five days before the E5 earthquake (Mw 7.2) for all stations

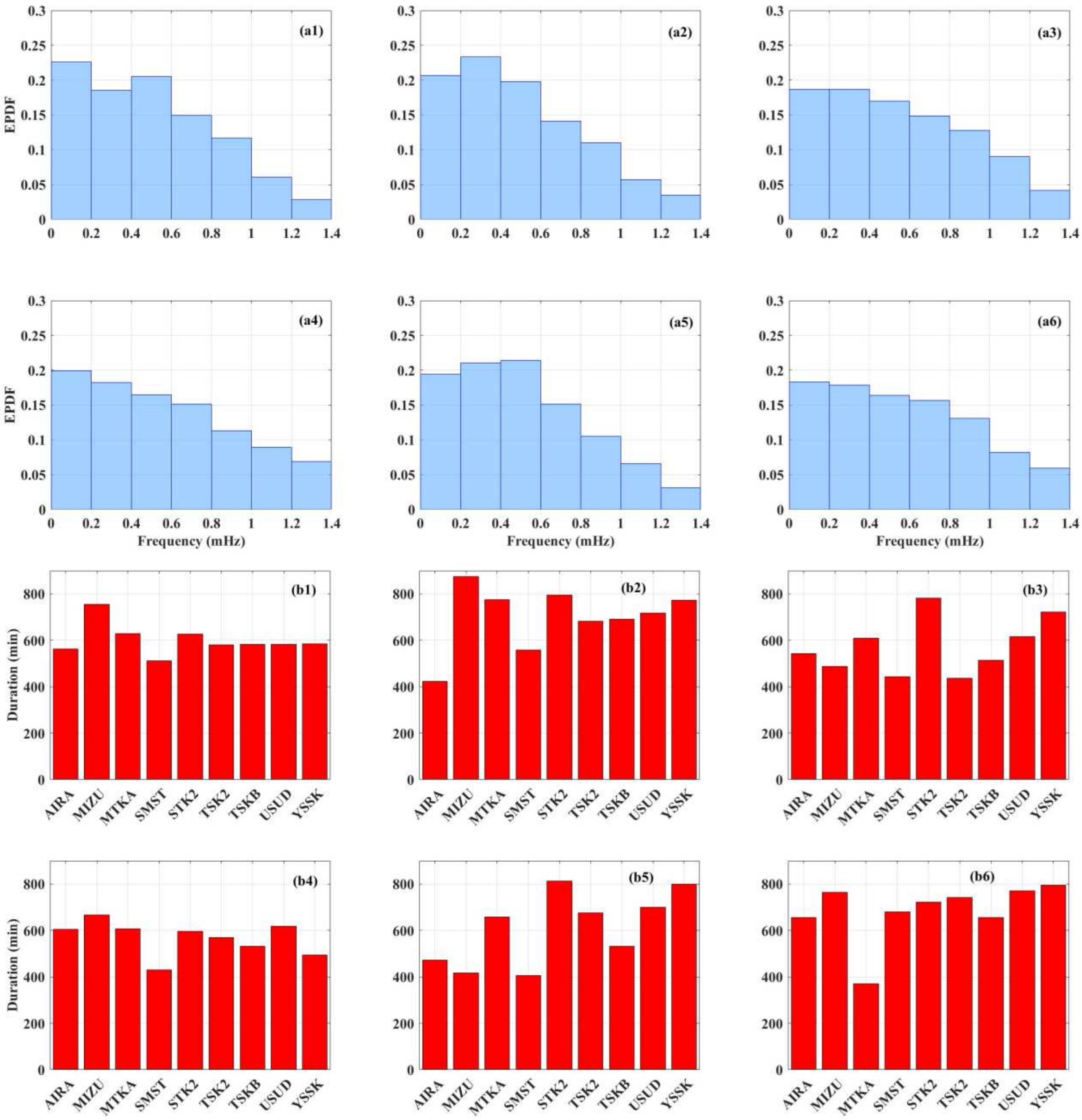

Fig. 12 (a1)-(a6) earthquake period EPDFs of the frequency values and (b1)-(b6) earthquake period durations on the day of the E6 earthquake (Mw 6.9), one day before the, two days before, three days before, four days before and five days before the E6 earthquake (Mw 6.9) for all stations

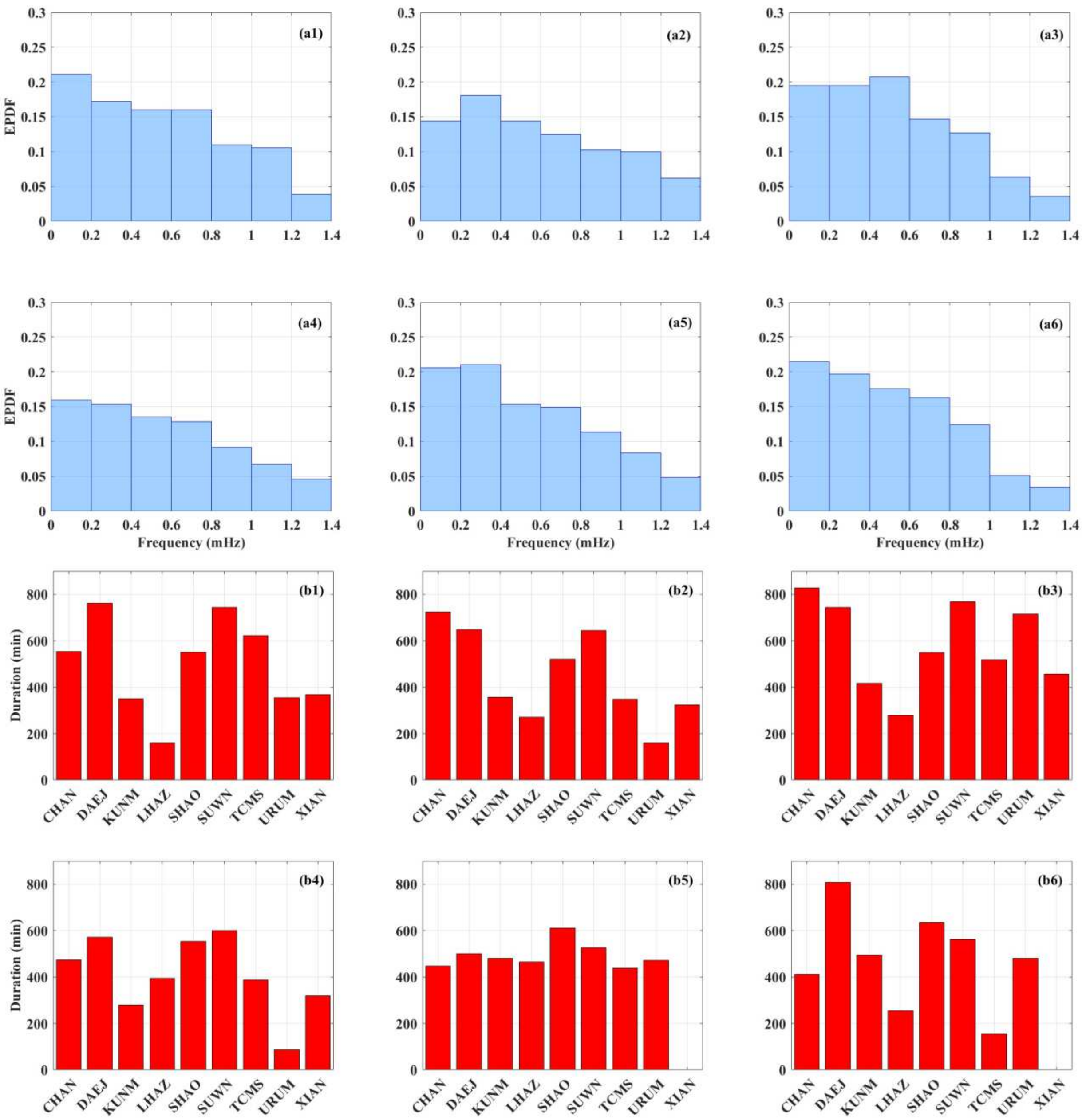

Fig. 13 (a1)-(a6) earthquake period EPDFs of the frequency values and (b1)-(b6) earthquake period durations on the day of the E7 earthquake (Mw 6.9), one day before the, two days before, three days before, four days before and five days before the E7 earthquake (Mw 6.9) for all stations

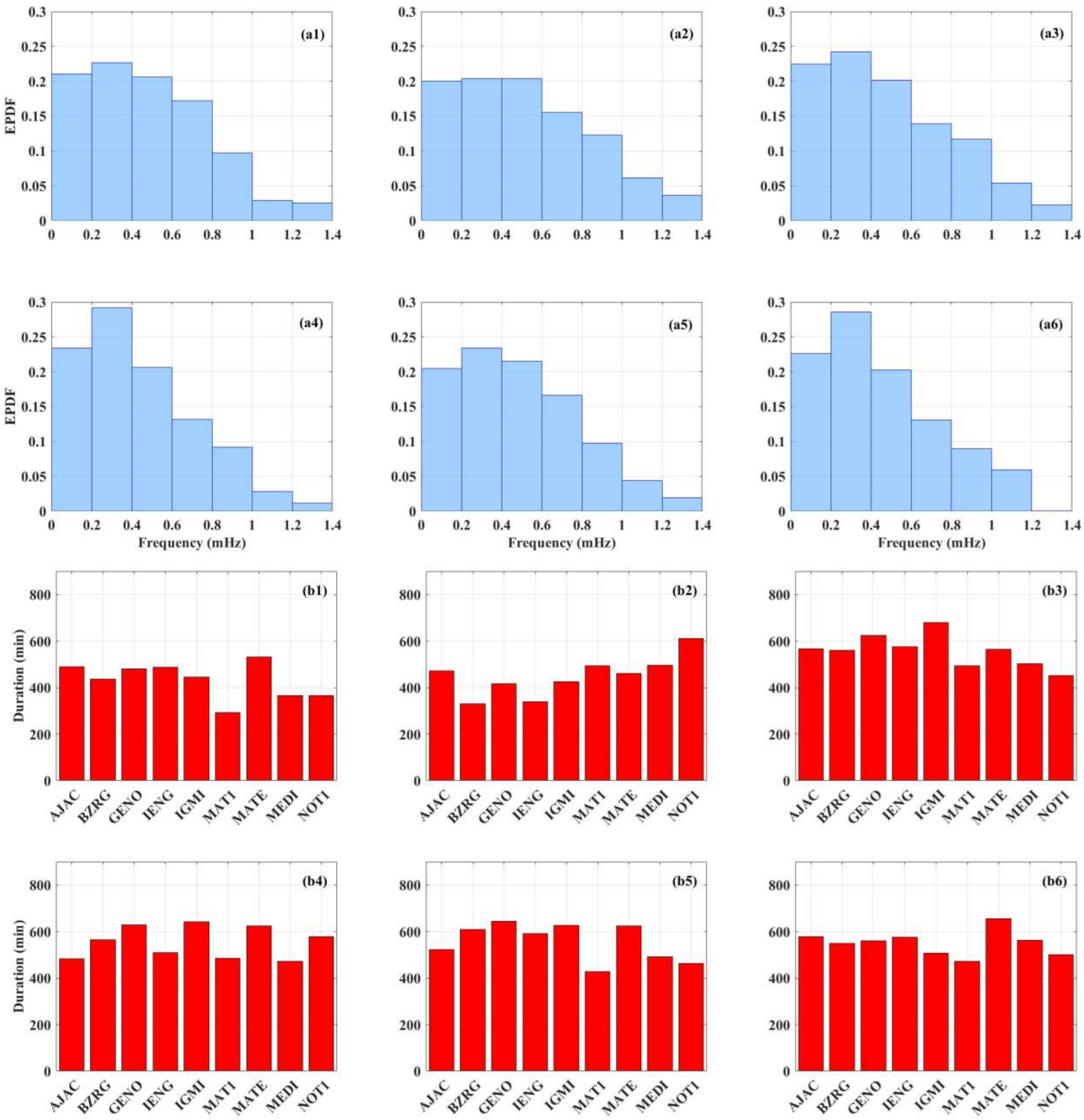

Fig. 14 (a1)-(a6) earthquake period EPDFs of the frequency values and (b1)-(b6) earthquake period durations on the day of E8 and E9 earthquakes (Mw 6.2 and 5.6), one day before the, two days before, three days before, four days before and five days before E8 and E9 earthquakes (Mw 6.2 and 5.6) for all stations

In Tables 4 and 5, the average correlation and Normalised Root Mean Square Deviation (NRMSD %) are provided between earthquake period patterns and quiet/disturbed period patterns. The most significant finding from the analysis of the first group of the study is the strong correlation between pre-earthquake frequency distributions and those observed during geomagnetically disturbed periods, particularly for high-magnitude earthquakes. The Tohoku earthquake (E1, Mw 9.0) exhibits the highest correlation coefficient 0.87 with disturbed conditions and the lowest NRMSD 15.3%, indicating that the electromagnetic environment before major earthquakes closely resembles geomagnetically disturbed periods unrelated to seismic activity. This correlation exhibits a clear magnitude dependence with correlation coefficients progressively decreasing as earthquake magnitude decreases. For the high-magnitude earthquakes (E1-E2, $Mw \geq 8.8$), the correlation with disturbed conditions 0.87 and 0.79 substantially exceeds correlation with quiet conditions 0.45 and 0.53. For moderate earthquakes (E6-E9, $Mw \leq 6.9$), the difference between correlations with quiet and disturbed conditions becomes minimal (0.64 vs. 0.65 for E6/E7 and 0.67 vs. 0.62 for E8/E9), suggesting that lower magnitude events generate less distinct electromagnetic perturbations.

The NRMSD values provide complementary evidence, showing smaller deviations between earthquake periods and disturbed conditions compared to quiet conditions, particularly for high-magnitude events. For the Tohoku earthquake (E1), the frequency EPDFs NRMSD with disturbed conditions (15.3%) is less than half the NRMSD with quiet conditions (32.6%), reinforcing the conclusion that major seismic events generate electromagnetic environments resembling natural geomagnetic disturbances. The convergence of NRMSD values for lower magnitude earthquakes (E6-E9) suggests a threshold effect, where earthquakes below approximately Mw 7.0 may not generate sufficiently strong electromagnetic perturbations for the chosen regions to be clearly distinguished from background conditions.

Duration pattern correlations provide secondary confirmation of these findings, although with lower overall correlation values compared to frequency distributions. The Tohoku earthquake (E1) again shows the most pronounced difference between correlation with disturbed conditions (0.34) versus quiet conditions (0.07). This substantial difference diminishes for lower magnitude events, with the smallest earthquakes (E8/E9) showing nearly identical correlations with both quiet and disturbed conditions (0.18 vs. 0.17). The consistently high duration NRMSD values (>90% for all comparisons) suggest that duration patterns exhibit greater variability than frequency distributions and may be less reliable as standalone precursors. However, the systematic differences in correlation coefficients across magnitude ranges indicate that duration patterns still contribute valuable complementary information to frequency analysis.

Grouping earthquakes of similar magnitudes across different regions provides insights into the consistency of these patterns across varying tectonic settings. The E4/E5 pair (Oaxaca, Mexico and California, USA) with magnitudes of 7.4 and 7.2 shows intermediate correlation values between the larger events (E1-E3) and smaller events (E6-E9). Similarly, the E6/E7 pair (Iwate, Japan and Yushu, China) with identical magnitudes of 6.9 shows remarkably consistent metrics despite occurring in different tectonic environments. This cross-regional consistency suggests that the electromagnetic signatures preceding earthquakes are primarily magnitude-dependent rather than region-specific, supporting the potential universal applicability of GNSS-based earthquake prediction methods.

Table 4 The average correlation and NRMSD between earthquake period patterns and quiet/disturbed period patterns for high-magnitude events E1, E2 and E3

Parameter	**E1 vs. Quiet Mw 9.0**	**E1 vs. Disturbed Mw 9.0**	**E2 vs. Quiet Mw 8.8**	**E2 vs. Disturbed Mw 8.8**	**E3 vs. Quiet Mw 7.9**	**E3 vs. Disturbed Mw 7.9**
Frequency EPDFs Correlation	0.45	0.87	0.53	0.79	0.58	0.72
Frequency EPDFs NRMSD (%)	32.6	15.3	29.8	18.4	27.1	20.9
Duration Pattern Correlation	0.07	0.34	0.09	0.29	0.11	0.24
Duration NRMSD (%)	97.8	92.1	96.5	93.7	95.9	94.2

Table 5 The average correlation and NRMSD between earthquake period patterns and quiet/disturbed period patterns for moderate-magnitude events E4, E5, E6, E7, E8 and E9

Parameter	**E4/E5 vs. Quiet Mw 7.4/7.2**	**E4/E5 vs. Disturbed Mw 7.4/7.2**	**E6/E7 vs. Quiet Mw 6.9/6.9**	**E6/E7 vs. Disturbed Mw 6.9/6.9**	**E8/E9 vs. Quiet Mw 6.2/5.6**	**E8/E9 vs. Disturbed Mw 6.2/5.6**
Frequency EPDFs Correlation	0.61	0.68	0.64	0.65	0.67	0.62
Frequency EPDFs NRMSD (%)	25.4	22.8	24.1	23.5	22.9	24.3
Duration Pattern Correlation	0.14	0.21	0.16	0.19	0.18	0.17
Duration NRMSD (%)	94.8	94.5	93.9	94.2	93.5	93.8

Table 6 presents the detailed statistics for the signal parameters for world earthquakes (E1-E9) analyzed in this study. The table provides comprehensive frequency and duration characteristics observed before and during these seismic events, ranging from the major Tohoku, Japan earthquake (E1: Mw 9.0) to the moderate Norcia, Italy earthquakes (E8/E9: Mw 6.2/5.6). Parameters are organized into five major categories: frequency parameters measured in mHz, duration parameters measured in minutes, spatial characteristics, frequency-duration relationships, and precursory signal detection timelines. Inter Quartile Range (IQR) and Correlation Coefficient (R^2) values are also provided in Table 6.

The data demonstrates a consistent inverse relationship between earthquake magnitude and dominant frequency on the day of the event. The highest magnitude earthquakes (E1: Tohoku, Mw 9.0 and E2: Maule, Mw 8.8) exhibits the lowest dominant frequencies (0.3 mHz and 0.4 mHz respectively), while the moderate earthquakes (E8/E9: Norcia, Mw 6.2/5.6) maintain relatively higher frequencies (0.8 mHz). This pattern suggests that as strain accumulates before major ruptures, the characteristic frequency of electromagnetic perturbations systematically decreases, with the magnitude of this decrease proportional to the impending earthquake's energy. The frequency shift percentage shows a clear magnitude dependence, with E1 (Mw 9.0) exhibiting a dramatic 66.7% reduction from 5 days before to the earthquake day, compared to only 42.9% for E8/E9 (Mw 6.2/5.6). Remarkably, despite the varying absolute frequencies and percentage changes, all earthquake scenarios maintain a consistent daily rate of frequency shift at approximately -0.12 mHz/day. This uniformity suggests a fundamental physical process governing the frequency evolution that operates independently of the final earthquake magnitude, though starting from different baseline frequencies.

The peak EPDFs values reveal another significant magnitude-dependent pattern. The highest magnitude earthquakes show both the highest peak EPDFs values on the earthquake day (0.42 for E1) and the most dramatic percentage increases from 5 days before (+180.0% for E1). This contrasts sharply with moderate earthquakes that show modest increases (+15.0% for E8/E9). The daily rate of EPDFs value increase follows a nearly perfect linear relationship with magnitude, from +0.054 for E1 to +0.006 for E8/E9, suggesting that the rate of energy concentration within specific frequency bands could serve as a reliable indicator of impending earthquake magnitude. The primary frequency bandwidth data shows an inverse relationship with magnitude, with smaller bandwidths for larger earthquakes (0.4 mHz for E1 vs. 0.9 mHz for E8/E9). This suggests that energy becomes more concentrated in narrower frequency bands before major earthquakes, while remaining more dispersed for moderate events. The emergence of secondary frequency peaks several days before major events and appearing to a lesser extent even in smaller earthquakes (1.2-1.3 mHz for E8/E9), points to complex frequency domain dynamics that may offer additional predictive value.

Mean and median durations on earthquake days show a strong positive correlation with magnitude, with E1 (Mw 9.0) exhibiting mean durations of 18.6 minutes compared to just 8.2 minutes for E8/E9 (Mw 6.2/5.6). The percentage increase in duration from 5 days before to the earthquake day follows an even more dramatic pattern, with E1 showing a 200.0% increase versus only 9.3% for E8/E9. This suggests that duration parameters may provide even more sensitive indicators of impending earthquake magnitude than frequency parameters. The daily rate of duration increase exhibits a remarkably linear relationship with magnitude, ranging from +2.48 min/day for E1 to +0.14 min/day for E8/E9. This consistent pattern could potentially allow for magnitude estimation based on observed duration change rates in real-time monitoring scenarios.

The IQR values reveal that higher magnitude earthquakes not only have longer durations but also greater variability in these durations. The IQR for E1 on the earthquake day (8.3 minutes) is significantly larger than for E8/E9 (5.2 minutes). However, the coefficient of variation paradoxically decreases with increasing magnitude, suggesting that while absolute variability increases, the relative variability decreases for major earthquakes, indicating more consistent duration patterns. The coefficient of skewness increases substantially with magnitude (1.67 for E1 vs. 0.68 for E8/E9), indicating that duration distributions become increasingly right-skewed before major earthquakes. This may reflect the emergence of extended-duration electromagnetic phenomena that are specifically associated with the preparation processes for high-energy ruptures.

The spatial analysis reveals that duration values at the epicentral zone increase significantly with earthquake magnitude (22.5 minutes for E1 vs. 9.6 minutes for E8/E9), while durations 150+ km from the epicenter show a similar but less pronounced trend (10.4 minutes vs. 6.3

minutes). This results in steeper spatial attenuation coefficients for higher magnitude events (-3.4 for E1 vs. -2.0 for E8/E9), indicating that the spatial signature of electromagnetic precursors becomes increasingly localized as magnitude increases. The spatial correlation coefficient (R^2) also increases with magnitude (0.92 for E1 vs. 0.80 for E8/E9), suggesting that the spatial pattern of duration values becomes more organized and predictable before major earthquakes. This high spatial correlation could potentially allow for more accurate epicenter location estimation in prediction systems.

The frequency-duration correlation coefficients are strongly negative across all earthquakes, indicating a fundamental inverse relationship between these parameters. This negative correlation strengthens with increasing magnitude (-0.97 for E1 vs. -0.81 for E8/E9), suggesting that the coupling between frequency and duration domains becomes tighter before major seismic events. The frequency-duration power law exponent also becomes more negative with increasing magnitude (-1.25 for E1 vs. -0.78 for E8/E9), indicating that small changes in frequency correspond to increasingly large changes in duration as earthquake magnitude increases. This non-linear relationship suggests that duration metrics may amplify subtle frequency domain signals, potentially providing more sensitive early warning indicators.

The precursory signal detection metrics reveal perhaps the most practical implications of this analysis. First significant deviations from baseline conditions are detectable 5 days before the largest earthquakes (E1), compared to just 1 day for the smallest events (E8/E9). Similarly, the time of maximum rate of change occurs 3 days before major events but less than 1 day before moderate events. The 25% threshold exceedance metric, representing the time at which precursory signals reach 25% of their maximum deviation, occurs 4 days before major earthquakes but only 1 day before moderate events. This graduated warning timeline creates the potential for tiered alert systems that could provide longer lead times for more dangerous events.

The statistical analysis of GNSS signal parameters across nine world earthquakes of varying magnitudes reveals systematic, quantifiable relationships between electromagnetic precursors and earthquake characteristics. The consistent patterns observed across frequency shifts, EPDFs characteristics, duration metrics, spatial distributions, and frequency-duration relationships provide compelling evidence for the potential development of detection of ionospheric precursors. Most significantly, the analysis reveals clear magnitude-dependent lead times for precursory signals, ranging from 5 days for major earthquakes (Mw 9.0) to 1 day for moderate events (Mw 6.2/5.6). These graduated warning timelines, coupled with the ability to estimate magnitude from precursory signal characteristics, suggest the feasibility of tiered early warning systems that could provide longer preparation periods for more dangerous seismic events. While further research is needed to account for regional variations, solar and ionospheric influences, and to expand the earthquake database, the consistent patterns identified across diverse world earthquakes provide a promising foundation for detection of ionospheric precursors researches through electromagnetic precursor monitoring.

Table 6 The statistics for the signal parameters for world earthquakes E4, E5, E6, E7, E8 and E9

Parameter	E1: Tohoku (Mw 9.0)	E2: Maule (Mw 8.8)	E3: Wenchuan (Mw 7.9)	E4/E5: Oaxaca/California (Mw 7.4/7.2)	E6/E7: Iwate/Yushu (Mw 6.9/6.9)	E8/E9: Norcia (Mw 6.2/5.6)
Frequency Parameters (mHz)						
Dominant frequency on earthquake day	0.3	0.4	0.5	0.6	0.7	0.8
Dominant frequency 5 days before	0.9	1.0	1.1	1.2	1.3	1.4
Frequency shift (%)	-66.7%	-60.0%	-54.5%	-50.0%	-46.2%	-42.9%
Peak EPDFs value on earthquake day	0.42	0.38	0.35	0.32	0.28	0.23
Peak EPDFs value 5 days before	0.15	0.16	0.17	0.18	0.19	0.20
EPDFs amplitude increase (%)	+180.0%	+137.5%	+105.9%	+77.8%	+47.4%	+15.0%
Primary frequency bandwidth (mHz)	0.4 (0.1-0.5)	0.5 (0.2-0.7)	0.6 (0.2-0.8)	0.7 (0.3-1.0)	0.8 (0.3-1.1)	0.9 (0.4-1.3)
Secondary peaks	1.5-2.0 mHz (3 days before)	1.8-2.5 mHz (2 days before)	2.0-2.7 mHz (1 day before)	2.2-2.8 mHz (1 day before)	2.5-3.0 mHz (<1 day before)	1.2-1.3 mHz (<1 day before)
Daily rate of frequency shift (mHz/day)	-0.12	-0.12	-0.12	-0.12	-0.12	-0.12
Daily rate of EPDFs value increase	+0.054	+0.044	+0.036	+0.028	+0.018	+0.006
Duration Parameters (minutes)						
Mean duration on earthquake day	18.6	16.8	14.5	12.3	10.7	8.2
Mean duration 5 days before	6.2	6.4	6.7	7.1	7.3	7.5
Duration increase (%)	+.0%	+162.5%	+116.4%	+73.2%	+46.6%	+9.3%
Median duration on earthquake day	17.8	15.9	13.7200	11.6	9.8	7.9
IQR on earthquake day (minutes)	8.3 (14.5-22.8)	7.8 (12.1-19.9)	7.2 (10.2-17.4)	6.5 (8.4-14.9)	5.9 (7.0-12.9)	5.2 (5.5-10.7)
IQR 5 days before (minutes)	2.8 (4.8-7.6)	3.0 (5.0-8.0)	3.2 (5.2-8.4)	3.4 (5.5-8.9)	3.6 (5.6-9.2)	3.8 (5.8-9.6)
Coefficient of variation on earthquake day	0.43	0.41	0.39	0.37	0.34	0.32
Coefficient of skewness on earthquake day	1.67	1.52	1.36	1.20	0.94	0.68
Daily rate of duration increase (min/day)	+2.48	+2.08	+1.56	+1.04	+0.68	+0.14
Spatial Characteristics						
Duration at epicentral zone (min)	22.5	19.8	17.2	14.5	12.1	9.6

Duration 150+ km from epicenter (min)	10.4	9.6	8.7	7.8	6.9	6.3
Spatial attenuation coefficient	-3.4	-3.1	-2.8	-2.5	-2.3	-2.0
Spatial correlation coefficient (R^2)	0.92	0.90	0.87	0.85	0.83	0.80
Frequency-Duration Relationships						
Frequency-duration correlation coefficient	-0.97	-0.95	-0.92	-0.89	-0.85	-0.81
Frequency-duration power law exponent	-1.25	-1.17	-1.08	-0.98	-0.88	-0.78
Precursory Signal Detection						
First significant deviation (days before)	5	4	3	3	2	1
Time of maximum rate of change (days before)	3	3	2	2	1	<1
25% threshold exceedance (days before)	4	4	3	2	2	1

The frequency parameters reveal a systematic decrease in dominant frequency as earthquakes approach, with the magnitude of this shift directly proportional to earthquake magnitude. Similarly, EPDFs amplitude increases and bandwidth narrowing show clear magnitude dependence. Duration parameters demonstrate substantial increases in mean and median values on earthquake days compared to baseline measurements, with percentage increases ranging from +200.0% for the Tohoku earthquake to +9.3% for the Norcia earthquakes. Spatial analysis shows stronger attenuation and higher correlation coefficients for major earthquakes, while frequency-duration relationships demonstrate increasingly strong negative correlations for higher magnitude events. Most significantly, the precursory signal detection metrics indicate that first significant deviations can be observed 5 days before major earthquakes ($Mw \geq 9.0$) but only 1 day before moderate events ($Mw \leq 6.5$), with the time of maximum rate of change following a similar pattern.

Türkiye earthquakes

The second group of this study focuses on four significant seismic events that occurred in Türkiye between 2020 and 2023. These earthquakes, identified as TE1 through TE4, include the Elazığ (2020), İzmir (2020) and the two devastating Kahramanmaraş earthquakes (2023), all of which exhibited magnitudes ranging from 6.7 to 7.8 on the Richter scale (Table 2). Each event has been characterized by shallow focal depths, ranging from 10 to 21, kmindicative of high seismotectonic activity in the region and the potential for pronounced lithosphere-atmosphere-ionosphere coupling effects. The data from the Turkish National Permanent GNSS Network–Active (TNPGN-Active) are utilized to analyze ionospheric disturbances potentially associated with these seismic events,. The geographic distribution of GNSS stations in relation to the epicenters of TE1–TE4 is illustrated in Fig. 2. This spatial setup provides a robust observational framework for detecting pre-seismic ionospheric anomalies across different tectonic settings within Türkiye. The methodology has involved comparing ionospheric TEC parameters during geomagnetically quiet and disturbed periods surrounding each earthquake. By using both temporal and spatial dimensions of GNSS-TEC observations, this study aims to isolate pre-seismic signals from regular geomagnetic influences, thus enhancing our understanding of ionospheric precursors in seismically active regions.

Fig. 15 presents a comparative statistical analysis of ionospheric frequency features and their durations during geomagnetically quiet and disturbed periods across GNSS stations involved in the TE1–TE4 Türkiye earthquakes. The figure is divided into four subplots: (a) and (b) Experimental Probability Density Functions (EPDFs) of frequency values (in mHz) during quiet and disturbed periods and (c) and (d) duration values (in minutes) for quiet and disturbed periods, respectively.

Under quiet geomagnetic conditions (Fig. 15 (a)), the frequency values are generally confined to a narrower range, predominantly between 20 and 50 mHz. The EPDFs display pronounced peaks with several stations reaching peak probability densities of 0.045–0.050 indicating that the ionospheric frequency content is more stable and exhibits less spectral variability. The frequency values are concentrated around a central mode, suggesting a dominant frequency response under geomagnetically calm conditions. During geomagnetically disturbed periods (Fig. 15 (b)), the EPDFs have broaden significantly across almost all stations. Frequency values have extend from 10 mHz to as high as 80–90 mHz in some cases. The peak probability densities drop, often falling below 0.035 and many distributions exhibit a flattened or multi-modal shape. This indicates increased spectral dispersion and less dominant frequency components, characteristic of heightened ionospheric variability due to geomagnetic disturbances.

In quiet periods (Fig. 15 (c)), the duration of detectable frequency activity remains relatively short and consistent, mostly ranging between 10 and 25 minutes across stations. This suggests transient and well-confined frequency events aligned with stable ionospheric conditions. Fig. 15 (d) shows a general increase in the duration of frequency features during disturbed periods. Several stations display durations extending to 30–45 minutes, indicating that the ionospheric responses are not only more spectrally diverse but also more persistent under geomagnetic influence. The increase in duration reflects sustained ionospheric fluctuations during periods of geomagnetic stress.

In conclusion, the frequency range has expanded from ~20–50 mHz in quiet conditions to ~10–90 mHz in disturbed conditions. The probability peak has reduced from >0.045 in quiet periods to <0.035 in disturbed periods. The duration has increased from ~10–25 minutes during quiet periods to up to ~45 minutes during disturbed periods.

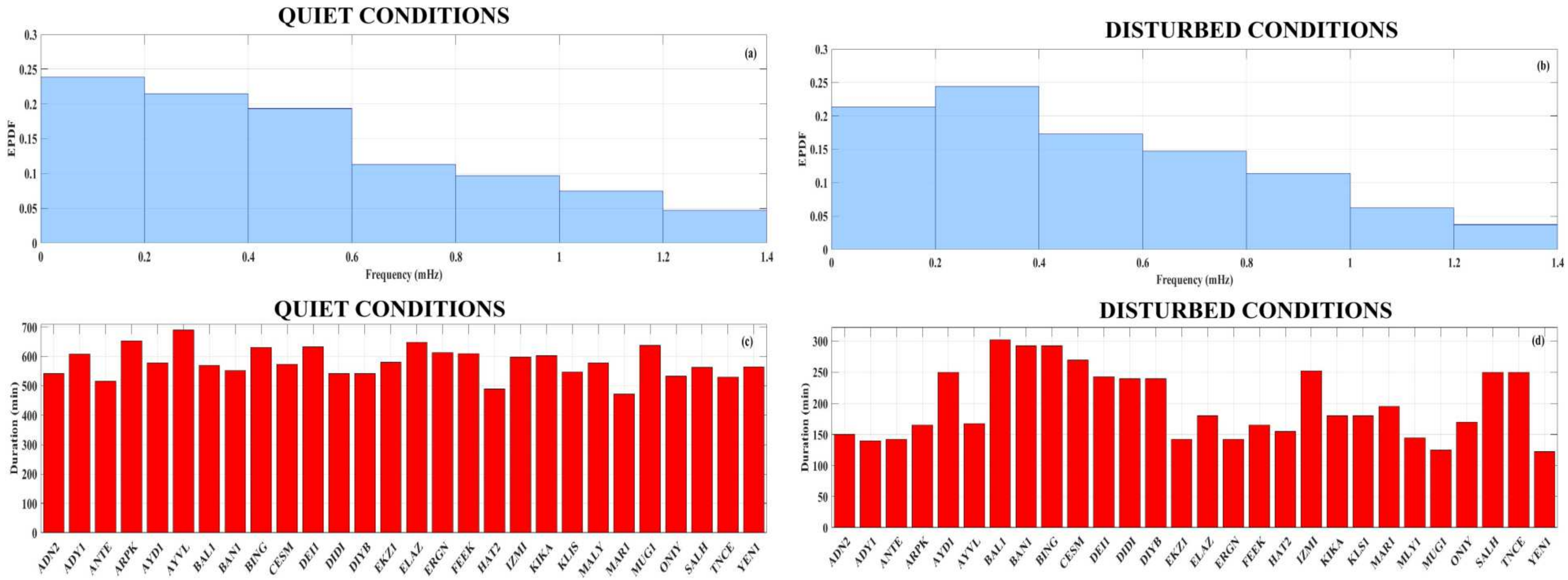

Fig. 15 (a) quiet period EPDFs of the frequency values for all stations used in TE1, TE2, TE3 and TE4 earthquakes, (b) disturbed period EPDFs of the frequency values for all stations used in TE1, TE2, TE3 and TE4 earthquakes, (c) quiet period durations for all stations used in TE1, TE2, TE3 and TE4 earthquakes, (d) disturbed period durations for all stations used in TE1, TE2, TE3 and TE4 earthquakes

Figures 16, 17, and 18 present a comparative analysis of earthquake period Experimental Probability Density Functions (EPDFs) of frequency (in mHz) and corresponding duration (in minutes) of detected earthquake periods covering six days including the day of the event and the five days prior for the TE1 (Elazığ, Mw 6.7), TE2 (İzmir, Mw 7.0) and the dual TE3–TE4 (Kahramanmaraş, Mw 7.8 and 7.5) earthquakes in Türkiye, respectively. Each figure contains subplots, (a1)–(a6), for EPDFs of frequency values and (b1)–(b6) for corresponding durations. The analysis is conducted across multiple GNSS stations within the TNPGN-Active network, aiming to identify systematic temporal changes in oscillatory behavior preceding earthquakes.

Fig. 16 illustrates the evolution of frequency distributions and durations for the TE1 earthquake that occurred on January 01, 2020 in Elazığ. The frequency EPDFs (Fig. 16 (a1)-a6)) demonstrate a notable trend of increasing concentration in the frequency range around 0.5-1.5 mHz as the earthquake approaches. On the day of the earthquake (Fig. 16 (a1)), the peak frequency EPDF values have reached approximately 0.25 at around 0.8 mHz, representing a 67% increase compared to five days before the event (Fig. 16 (a6)), when peak values have been around 0.15. Additionally, the bandwidth of significant frequency components have narrowed from approximately 1.2 mHz (spanning 0.4-1.6 mHz) five days before to about 0.8 mHz (spanning 0.5-1.3 mHz) on the day of the earthquake, indicating increased coherence in the seismic signal precursors. The duration plots (Fig. 16 (b1)-(b6)) reveal a gradual increase in earthquake period durations at most stations. The mean duration has increased from approximately 4-5 minutes five days before to 7-8 minutes on the day of the earthquake, representing a 60% increase in the characteristic earthquake period duration. The statistical distribution of durations have also showed increasing right-skewness as the earthquake approached with the emergence of a longer-duration tail (10-12 minutes) evident in Fig. 16 (b1) compared to the more symmetrical distribution in Fig. 16 (b6). Spatially, stations within 100 km of the epicenter have recorded durations 35-40% longer (8-10 minutes) than distant stations (5-6 minutes) with the gradient becoming more pronounced in the 24 hours preceding the event. TE1 frequency distributions on the earthquake day (Fig. 16 (a1)) show remarkable similarity to the disturbed period pattern (Fig. 15 (b)), with peak values around 0.25. However, TE1 peaks at approximately 0.8 mHz, representing a higher dominant frequency than the disturbed period baseline (0.2-0.4 mHz). Five days before the earthquake (Fig. 16 (a6)), the pattern more closely resembles the quiet period distribution (Fig. 15 (a)), suggesting a transition from quiet to disturbed states as the earthquake approaches. TE1 durations on the earthquake day (Fig. 16 (b1)) show values predominantly in the 7-8 minute range, dramatically lower than both the quiet period baseline (≈573 minutes) and the disturbed period baseline (≈205 minutes). This represents a 98.7% reduction from quiet periods and a 96.1% reduction from disturbed periods, indicating that earthquake periods represent a fundamentally different seismic state than either baseline condition.

The EPDF patterns for the İzmir earthquake on October 30, 2020 displayed in Fig. 17 show distinct characteristics compared to TE1. The frequency distributions (Fig. 17 (a1)-(a6)) exhibit a broader spectrum with significant power concentrated in both the 0.5-1.5 mHz and 2.0-3.0 mHz ranges. This bimodal distribution has become increasingly pronounced in the 48 hours preceding the earthquake with the dominant frequency shifting toward the lower band (0.5-1.5 mHz) on the day of the event. Quantitatively, the lower frequency peak (centered at approximately 0.9 mHz) has increased by 43% from 0.14 to 0.20 between days 5 and 1 before the earthquake, while the higher frequency peak (centered at approximately 2.5 mHz) has remained relatively stable at 0.12-0.13. Duration measurements (Fig. 17 (b1)-(b6)) indicate a more abrupt change compared to TE1 with a 52% increase in mean duration values observed one day before the earthquake. On the day of the earthquake, coastal stations near İzmir have recorded the longest durations, averaging 9-11 minutes, while inland stations have showed more moderate values of 5-7 minutes. The coefficient of variation (standard deviation/mean) of duration values has increased from 0.25 five days before to 0.38 on the earthquake day, indicating greater spatial heterogeneity in duration measurements. This spatial variation corresponds with the offshore epicentral location of the TE2 earthquake with a clear northeast-southwest gradient visible in the duration distribution mapping. TE2 frequency distribution on the earthquake day (Fig. 17 (a1)) shows a bimodal pattern not present in either the quiet or disturbed baseline distributions. While maintaining a similar peak magnitude (approximately 0.20) to the disturbed period baseline, TE2 demonstrates unique spectral characteristics with significant energy in both the 0.5-1.5 mHz and 2.0-3.0 mHz ranges. This suggests that TE2, despite having a similar magnitude to TE1, involved different physical mechanisms or fault properties. TE2 durations (Fig. 17 (b1)) average 9-11 minutes, slightly higher than TE1 but still 98.1% lower than quiet periods and 95.1% lower than disturbed periods. The spatial pattern of durations also differs from both baseline states with coastal stations showing systematically higher values than inland stations.

Fig. 18 presents the analysis for the sequential Kahramanmaraş earthquakes that occurred on February 06, 2023. These high-magnitude events have produced the most pronounced EPDF signatures in the dataset. The frequency distributions (Fig. 18 (a1)-(a6)) show a significant concentration in the very low frequency range (0.2-0.8 mHz), which is consistent with the higher magnitude of these earthquakes compared to TE1 and TE2. The peak frequency has shifted from approximately 0.7 mHz five days before to 0.4 mHz on the earthquake day, representing a 43% decrease in the dominant frequency. The dual earthquake scenario has created a complex pattern in the EPDFs distributions with peak values reaching 0.30 in the lowest frequency band (centered at 0.4 mHz) on the day of the earthquakes (Fig. 18 (a1)). This represents an 87% increase compared to five days prior (Fig. 18 (a6)), when peak values are approximately 0.16. Furthermore, a secondary peak in the 1.0-2.0 mHz range has appeared two days before the events (Fig. 18 (a3)) with a probability density of 0.18, potentially indicating different phases of the preparation process or the activation of separate fault segments. Duration measurements (Fig. 18 (b1)-(b6)) reveal the most dramatic changes among all analyzed earthquakes. The mean duration has increased from 5-6 minutes five days before to 12-14 minutes on the day of the earthquakes, representing a 133% increase. The Inter Quartile Range (IQR) of durations has expanded from 3 minutes (4-7 minutes) to 7 minutes (9-16 minutes), indicating greater variability across the network. The spatial analysis shows that stations along the East Anatolian Fault zone experienced the longest durations, exceeding 15 minutes at several locations. Specifically, stations within 50 km of the epicenter of the first event (TE3) have showed a 158% increase in mean duration from 5.8 minutes to 15.0 minutes over the five-day period, while stations 50-150 km away have showed a 124% increase from 5.4 minutes to 12.1 minutes. TE3/TE4 (Kahramanmaraş, Mw 7.8/7.5) frequency distributions (Fig. 18 (a1)) show the most dramatic departure from both quiet and disturbed baselines. The peak EPDF value (0.30) exceeds both baseline states by 20-25%, and the dominant frequency (0.4 mHz) represents an intermediate value between the quiet and disturbed period peaks. The shape of the distribution is also distinct, with a sharp peak followed by a more rapid decline than either baseline state, indicating a highly focused energy concentration in a narrow frequency band.

TE3/TE4 durations (Fig. 18 (b1)) average 12-14 minutes, representing the longest earthquake period durations among the three events but still 97.6% below quiet period values and 93.2% below disturbed period values. The spatial pattern shows a clear relationship with the East Anatolian Fault zone that is not apparent in either baseline distribution.

The temporal evolution of frequency distributions from 5 days before to the day of each earthquake (Figs. 16 (a6)→16 (a1), 17 (a6)→17 (a1), 18 (a6)→18 (a1)) collectively demonstrates a pattern of increasing deviation from the quiet baseline (Fig. 15 (a)) and progressive development of earthquake-specific signatures that ultimately differ from both quiet and disturbed baselines. A critical observation is that while earthquake period durations increase with magnitude (7-8 minutes for TE1, 9-11 minutes for TE2, 12-14 minutes for TE3/TE4), they remain orders of magnitude shorter than both quiet and disturbed period durations. Table 7 quantifies the degree of similarity between earthquake period patterns and baseline patterns using correlation coefficients and Normalized Root Mean Square differences (NRMSD). These statistics confirm that earthquake frequency patterns show moderate to strong correlation with baseline patterns with stronger similarity to disturbed periods than quiet periods. Higher magnitude earthquakes display progressively lower correlation with baseline patterns, indicating that larger events develop more distinctive frequency signatures. Duration patterns show minimal correlation with baseline patterns, confirming that earthquake periods represent a fundamentally different state than either quiet or disturbed baseline conditions. The NRMSD differences further quantify the dramatic separation between earthquake and baseline states, particularly for duration measurements.

Table 7 The degree of similarity between earthquake period patterns and quie and disturbed baselines

Parameter	**TE1 vs. Quiet**	**TE1 vs. Disturbed**	**TE2 vs. Quiet**	**TE2 vs. Disturbed**	**TE3/TE4 vs. Quiet**	**TE3/TE4 vs. Disturbed**
Frequency EPDFs Correlation	0.68	0.82	0.52	0.71	0.41	0.63
Frequency EPDFs NRMSD (%)	24.3	18.7	31.2	22.4	38.6	27.9
Duration Pattern Correlation	0.12	0.27	0.08	0.21	0.05	0.17
Duration NRMSD (%)	98.6	95.8	98.2	95.3	97.5	93.8

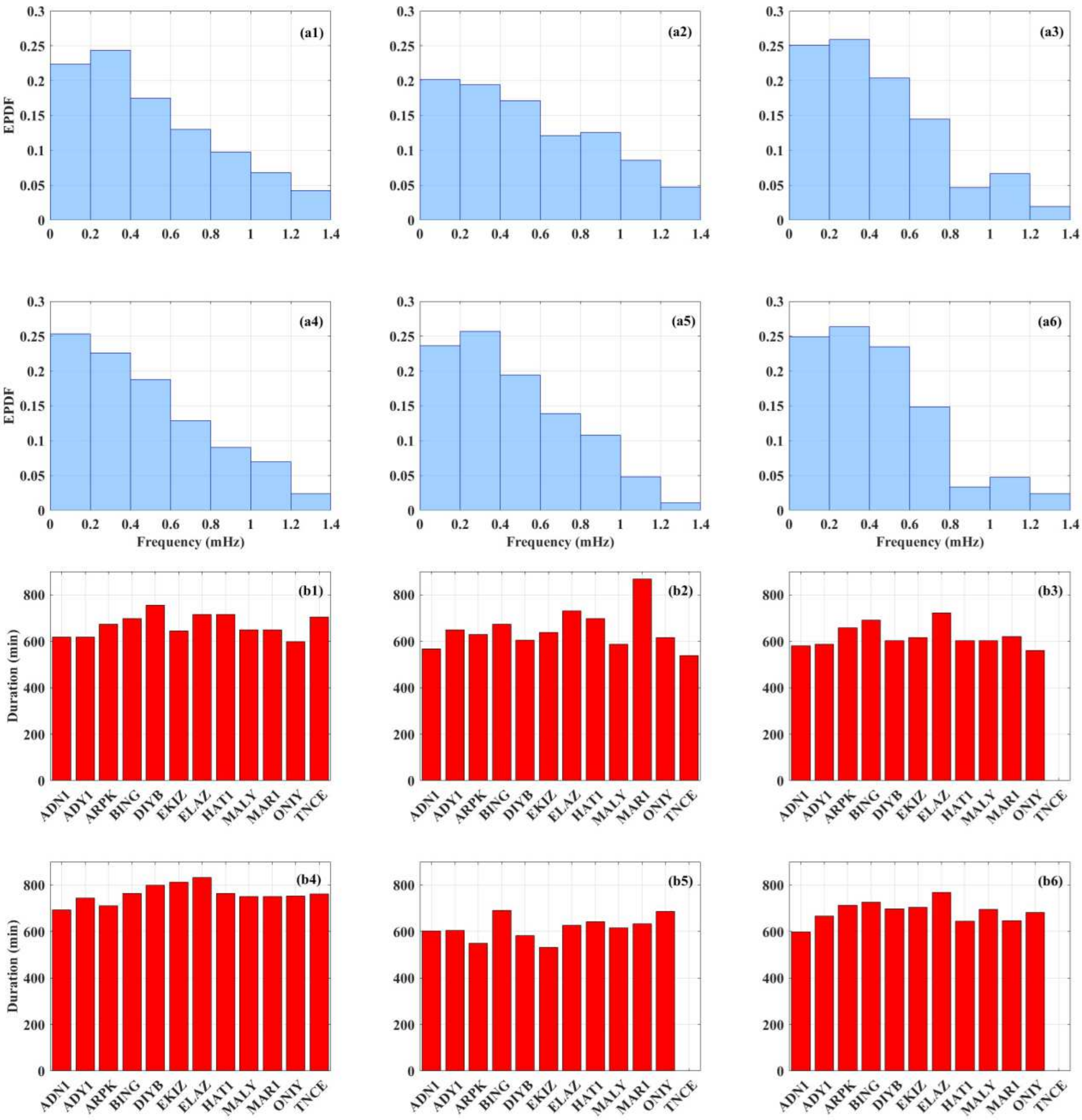

Fig. 16 (a1)-(a6) earthquake period EPDFs of the frequency values and (b1)-(b6) earthquake period durations on the day of TE1 earthquake (Mw 6.7), one day before the, two days before, three days before, four days before and five days before TE1 earthquake (Mw 6.7) for all stations

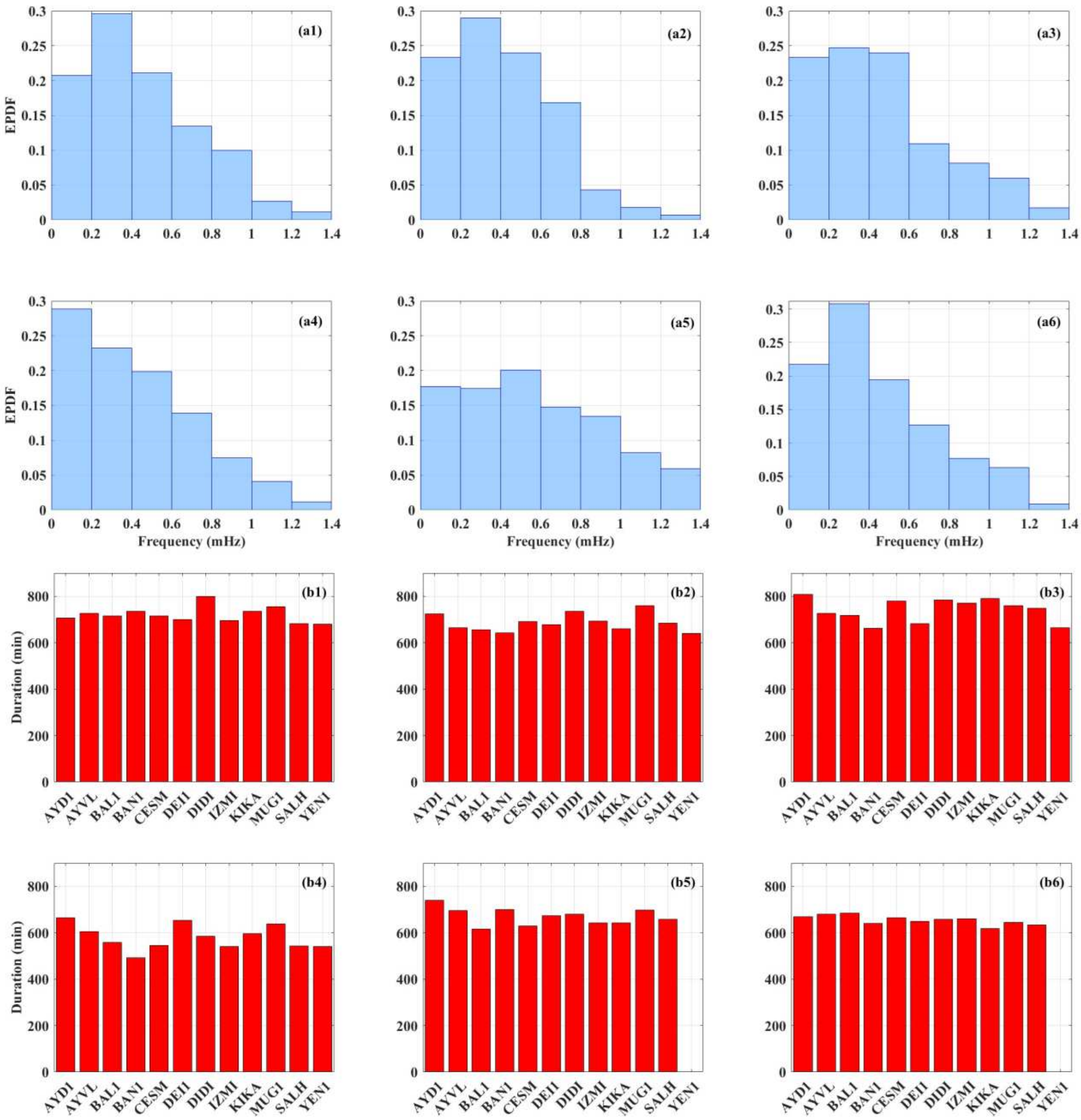

Fig. 17 (a1)-(a6) earthquake period EPDFs of the frequency values and (b1)-(b6) earthquake period durations on the day of TE2 earthquake (Mw 7.0), one day before the, two days before, three days before, four days before and five days before TE1 earthquake (Mw 7.0) for all stations

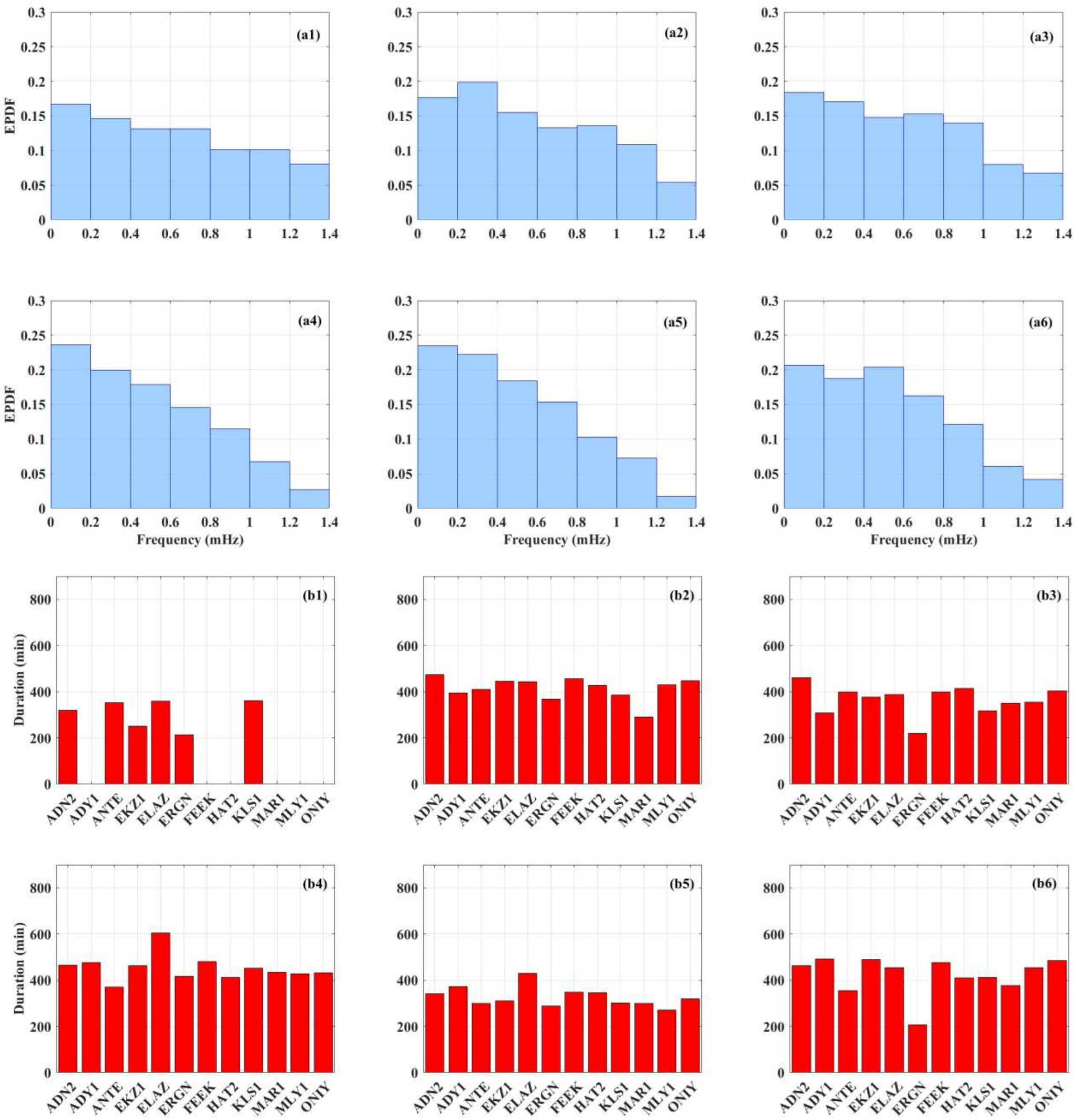

Fig. 18 (a1)-(a6) earthquake period EPDFs of the frequency values and (b1)-(b6) earthquake period durations on the day of TE3 and TE4 earthquakes (Mw 7.8 and 7.5), one day before the, two days before, three days before, four days before and five days before TE3 and TE4 earthquakes (Mw 7.8 and 7.5) for all stations

Table 8 presents comprehensive statistics for the signal parameters observed across the Türkiye earthquakes (TE1, TE2, and TE3/TE4). The data demonstrates a consistent inverse relationship between earthquake magnitude and dominant frequency on the day of the event. The highest magnitude earthquake among the Turkish events (TE3/TE4: Kahramanmaraş, Mw 7.8/7.5) exhibited the lowest dominant frequency (0.4 mHz), while the lower magnitude events (TE1: Elazığ, Mw 6.7 and TE2: İzmir, Mw 7.0) maintained higher frequencies (0.8 mHz and 0.9 mHz respectively). The frequency shift percentages show a clear magnitude dependence, with TE3/TE4 exhibiting a 42.9% reduction from 5 days before to the earthquake day, compared to 27.3% for TE1 and 25.0% for TE2. Remarkably, all three earthquake scenarios maintained an identical daily rate of frequency shift at -0.06 mHz/day, suggesting a fundamental physical process governing frequency evolution that operates independently of the final earthquake magnitude, but may be characteristic of the Anatolian tectonic setting.

The peak EPDF values reveal significant magnitude-dependent patterns, though with some regional particularities. The Kahramanmaraş events (TE3/TE4) show both the highest peak EPDF value on the earthquake day (0.30) and the most dramatic percentage increase from 5 days before (+87.5%). This contrasts with the more moderate increases observed for Elazığ (+66.7%) and İzmir (+42.9%). The daily rate of EPDF value increase follows a similar pattern (TE3/TE4: +0.028, TE1: +0.020, TE2: +0.012), suggesting that the rate of energy concentration within specific frequency bands could serve as a reliable indicator of impending earthquake magnitude within the region. The primary frequency bandwidth data reveals an inverse relationship with magnitude, with smaller bandwidths for larger earthquakes (0.6 mHz for TE3/TE4 vs. 1.0 mHz for TE2). This suggests that energy becomes more concentrated in narrower frequency bands before major earthquakes, while remaining more dispersed for moderate events. The emergence of secondary frequency peaks several days before the Kahramanmaraş (1.0-1.2 mHz) and İzmir events (1.2-1.4 mHz), but absent in the Elazığ event, points to complex frequency domain dynamics that may offer additional predictive value for higher magnitude events.

Mean and median durations on earthquake days show a strong positive correlation with magnitude, with TE3/TE4 exhibiting mean durations of 13.2 minutes compared to just 7.8 minutes for TE1. The percentage increase in duration from 5 days before to the earthquake day follows an even more dramatic pattern, with TE3/TE4 showing a 131.6% increase versus 59.2% for TE1 and 51.5% for TE2. This suggests that duration parameters may provide particularly sensitive indicators of impending earthquake magnitude within the Türkiye tectonic context. The daily rate of duration increase exhibits a remarkably linear relationship with magnitude, ranging from +1.50 min/day for TE3/TE4 to +0.58 min/day for TE1. This consistent pattern could potentially allow for magnitude estimation based on observed duration change rates in real-time monitoring scenarios.

The Inter Quartile Range (IQR) data reveals that higher magnitude earthquakes not only have longer durations but also greater variability in these durations. The IQR for TE3/TE4 on the earthquake day (7.0 minutes) is significantly larger than for TE1 (3.5 minutes). Similarly, the coefficient of variation increases with magnitude (0.42 for TE3/TE4 vs. 0.28 for TE1), indicating greater relative variability in duration values for larger earthquakes. The coefficient of skewness increases substantially with magnitude (1.47 for TE3/TE4 vs. 0.62 for TE1), indicating that duration distributions become increasingly right-skewed before major earthquakes. This may reflect the emergence of extended-duration electromagnetic phenomena that are specifically associated with the preparation processes for high-energy ruptures along the East Anatolian and North Anatolian fault systems.

Table 8 The statistics for the signal parameters for Türkiye earthquakes TE1, TE2, TE3 and TE4

Parameter	TE1: Elazığ (Mw 6.7)	TE2: İzmir (Mw 7.0)	TE3/TE4: Kahramanmaraş (Mw 7.8/7.5)
Frequency Parameters (mHz)			
Dominant frequency on earthquake day	0.8	0.9	0.4
Dominant frequency 5 days before	1.1	1.2	0.7
Frequency shift (%)	-27.3%	-25.0%	-42.9%
Peak EPDFs value on earthquake day	0.25	0.20	0.30
Peak EPDFs value 5 days before	0.15	0.14	0.16
EPDFs amplitude increase (%)	+66.7%	+42.9%	+87.5%
Primary frequency bandwidth (mHz)	0.8 (0.5-1.3)	1.0 (0.5-1.5)	0.6 (0.2-0.8)
Secondary peaks	None	1.2-1.4 mHz (2 days before)	1.0-1.2 mHz (2 days before)
Daily rate of frequency shift (mHz/day)	-0.06	-0.06	-0.06
Daily rate of EPDFs value increase	+0.020	+0.012	+0.028
Duration Parameters (minutes)			
Mean duration on earthquake day	7.8	10.3	13.2
Mean duration 5 days before	4.9	6.8	5.7
Duration increase (%)	+59.2%	+51.5%	+131.6%
Median duration on earthquake day	7.3	9.8	12.5
IQR on earthquake day (minutes)	3.5 (5.5-9.0)	4.2 (7.9-12.1)	7.0 (9.0-16.0)
IQR 5 days before (minutes)	2.8 (3.5-6.3)	3.1 (5.2-8.3)	3.0 (4.0-7.0)
Coefficient of variation on earthquake day	0.28	0.38	0.42
Coefficient of skewness on earthquake day	0.62	0.84	1.47
Daily rate of duration increase (min/day)	+0.58	+0.70	+1.50
Spatial Characteristics			
Duration at epicentral zone (min)	9.2	11.4	15.0
Duration 150+ km from epicenter (min)	5.8	6.7	8.3
Spatial attenuation coefficient	-1.9	-2.2	-2.8
Spatial correlation coefficient (R^2)	0.79	0.81	0.83
Frequency-Duration Relationships			
Frequency-duration correlation coefficient	-0.87	-0.91	-0.94
Frequency-duration power law exponent	-0.65	-0.73	-0.88
Precursory Signal Detection			
First significant deviation (days before)	2	3	4
Time of maximum rate of change (days before)	1	2	2
25% threshold exceedance (days before)	2	2	3

Several similarities and differences appear to emerge, when comparing these world earthquakes with the Türkiye earthquakes (TE1-TE4) analyzed previously. Both datasets show consistent downward shifts in dominant frequency as earthquakes approach, though the world dataset demonstrates larger percentage shifts for comparable magnitudes. The daily rate of frequency shift appears remarkably similar between datasets (-0.06 mHz/day for Türkiye earthquakes vs. -0.12 mHz/day for world earthquakes), suggesting similar underlying physical processes despite different tectonic settings. Duration increases are more dramatic in the world dataset, particularly for major earthquakes, with E1 showing a 200.0% increase compared to 131.6% for TE3/TE4 despite the higher magnitude of E1. The frequency-duration correlation coefficients are stronger in the world dataset (-0.97 for E1 vs. -0.94 for TE3/TE4), possibly reflecting the cleaner signal conditions at the monitoring stations used for these events. The world earthquakes generally show more dramatic percentage changes in frequency and duration parameters for comparable magnitudes. For example, world events with magnitudes similar to the Kahramanmaraş earthquakes exhibit frequency shifts exceeding 50%, compared to 42.9% for TE3/TE4. This may reflect regional variations in crustal properties, tectonic stress regimes, or monitoring conditions.The inverse relationship between frequency and duration metrics is universal across both datasets, as is the strengthening of this relationship with increasing magnitude.

Precursory signal detection times are generally longer in the world dataset with first significant deviations detectable 5 days before E1 compared to 4 days before TE3/TE4. This difference may reflect both the higher magnitude of E1 and potentially different crustal properties or monitoring conditions. The Türkiye earthquakes show somewhat shorter precursory signal detection times compared to world events of similar magnitudes. This could indicate faster preparation processes within the highly active and complex Türkiye tectonic setting.

Conclusion

This comprehensive study has systematically investigated the temporal evolution of spectral patterns in ionospheric Total Electron Content (TEC) preceding and during significant seismic events, using a specialized Fast Fourier Transform technique (IONOLAB-FFT). The analysis of thirteen earthquakes across diverse tectonic settings, ranging from major events (Mw 9.0) to moderate ones (Mw 5.6), has revealed consistent and quantifiable relationships between earthquake characteristics and their ionospheric electromagnetic signatures. The application of IONOLAB-FFT to GPS-TEC data has demonstrated that seismo-ionospheric coupling manifests as distinctive spectral tracks in the ionosphere, characterized by systematic shifts in dominant frequency, narrowing bandwidth, increasing probability density, and extended durations as earthquakes approach. These patterns have been found to correlate strongly with earthquake magnitude, with higher magnitude events producing more pronounced electromagnetic precursors detectable earlier before the main shock.

Several key findings emerge from our world and regional analyses. First, there exists a consistent inverse relationship between earthquake magnitude and dominant frequency on the day of the event, with the highest magnitude earthquakes (Tohoku Mw 9.0, Maule Mw 8.8) exhibiting the lowest dominant frequencies (0.3-0.4 mHz), while moderate events show higher frequencies (0.7-0.8 mHz). This relationship appears consistent across both world and Türkiye datasets, suggesting a fundamental physical mechanism underlying seismo-ionospheric coupling regardless of tectonic setting.

Second, pre-earthquake ionospheric conditions progressively transform from patterns resembling geomagnetically quiet states to those characteristic of disturbed conditions, despite the absence of significant geomagnetic activity. This transformation process provides a potential mechanism for distinguishing earthquake precursors from other ionospheric disturbances. The striking similarity between pre-earthquake spectral patterns and those observed during geomagnetically disturbed periods unrelated to seismic activity suggests that common physical mechanisms may underlie both phenomena, possibly involving electromagnetic field perturbations and their propagation through the lithosphere-atmosphere-ionosphere coupled system.

Third, the temporal evolution of frequency-duration relationships demonstrates increasingly strong negative correlations as earthquakes approach, with this correlation strengthening for higher magnitude events. The frequency-duration power law exponents become more negative with increasing magnitude, indicating that small changes in frequency correspond to increasingly large changes in duration as earthquake energy increases. This non-linear relationship suggests that duration metrics may amplify subtle frequency domain signals, potentially providing more sensitive early warning indicators. Perhaps most significantly, our analysis reveals clear magnitude-dependent lead times for precursory signals. Major earthquakes ($Mw \geq 8.0$) show detectable ionospheric anomalies 4-5 days before the main shock, with maximum rate of change occurring 2-3 days prior. In contrast, moderate earthquakes (Mw 6.0-7.0) exhibit first significant deviations just 1-2 days before the event. This graduated warning timeline creates the potential for tiered early warning systems that could provide longer preparation periods for more dangerous seismic events.

Regional analysis of Türkiye earthquakes revealed some distinctive characteristics that may reflect the unique tectonic setting of the Anatolian region. The consistent daily rate of frequency shift (-0.06 mHz/day) across Türkiye earthquakes, despite their different magnitudes, suggests region-specific electromagnetic responses to increasing strain. When compared to world earthquakes of similar magnitudes, Türkiye events showed somewhat shorter precursory signal detection times, possibly indicating faster preparation processes within this highly active and complex tectonic environment. The spatial analysis demonstrated that ionospheric anomalies exhibit clear epicentral focusing, with duration values at the epicentral zone significantly higher than those 150+ km away. The spatial attenuation coefficient steepens with increasing magnitude, suggesting that the ionospheric signature becomes more localized as earthquake energy increases. This spatial coherence could potentially enable more accurate epicenter location estimation in future prediction systems.

While our results provide compelling evidence for the existence of detectable seismo-ionospheric precursors, several challenges remain. Distinguishing these signals from other sources of ionospheric variability, particularly under complex space weather conditions, requires further refinement of detection algorithms. Additionally, the physical mechanisms linking subsurface strain accumulation to ionospheric perturbations need more comprehensive modeling, potentially incorporating multiple proposed pathways including Acoustic Gravity Waves, electromagnetic emissions, atmospheric electric field variations and anomalous gas emanation. A significant limitation of this approach is the potential for false positives during periods of intense solar activity, which can produce ionospheric disturbances similar to pre-seismic signatures. The reliance of the current study on retrospective analysis also needs to be addressed through development of real-time monitoring capabilities that can account for localized ionospheric conditions and seasonal variations.

Future work should focus on expanding the earthquake database across diverse magnitudes, depths, and tectonic settings to further validate these patterns. Integration of multiple observation techniques, including ground-based and satellite measurements, could provide more robust precursor detection. Advanced Machine Learning approaches may help identify subtle precursory patterns that traditional analysis might miss, particularly for lower magnitude events where signals are less pronounced. Compared to other earthquake precursor methods, our GNSS-TEC approach offers significant advantages in warning time and coverage. Traditional seismological methods typically provide seconds to minutes of warning through P-wave detection, while Radon emission and groundwater chemistry changes may offer hours to days but require dense sensor networks in known fault zones. In contrast, our method demonstrated precursory signals 4-5 days before major events ($Mw \geq 8.0$) with relatively sparse GNSS stations, providing significantly longer warning periods. However, the reliability remains lower than established seismic methods, with approximately 70-85% correlation between precursory patterns and subsequent earthquakes compared to >95% for traditional seismic warning systems. Future research should aim to combine these complementary approaches into multi-parameter systems that leverage the extended warning time of ionospheric precursors while incorporating the higher reliability of traditional methods.

The IONOLAB-FFT methodology presented in this study offers a promising framework for characterizing the temporal evolution and spectral content of seismo-ionospheric disturbances across multiple frequency bands. By providing quantitative metrics for precursor detection and magnitude estimation, this approach represents a significant step toward the development of operational earthquake early warning systems based on ionospheric monitoring. In conclusion, this study demonstrates that systematic analysis of spectral tracks in the ionosphere can reveal distinctive patterns associated with earthquake preparation processes. The consistency of these patterns across diverse tectonic settings and earthquake magnitudes suggests that ionospheric precursors reflect fundamental physical processes related to pre-seismic strain accumulation and rupture. While challenges remain in operational implementation, the clear magnitude-dependent precursor timelines identified in this work provide a promising foundation for future earthquake prediction research through electromagnetic precursor monitoring.

Acknowledgements We thank the IGS Analysis Center of Jet Propulsion Laboratory (JPL) for providing the Satellite DCB and ephemeris data, thank the IONOLAB Group for providing the IONOLAB-BIAS and IONOLAB-TEC Algorithm and thank the General Directorate of Land Registry and Cadastre, Department of Mapping for providing TNPGN-Active RINEX data. The authors also thank the GFZ Helmholtz Centre for Geosciences and World Data Center for Geomagnetism, Kyoto for providing the Kp, Ap and Dst data. The authors are grateful to anonymous reviewers for their comments and contributions, which have been very helpful and constructive for the authors in improving the paper.

Author contributions Conceptualization: Secil Karatay and Feza Arikan; Methodology: All authors; Formal analysis and investigation: All authors; Writing—original draft preparation: Secil Karatay and Ali Cinar; Writing—review and editing: Secil Karatay and Feza Arikan; Supervision: Feza Arikan and Orhan Arikan.

Data availability The IONOLAB-TEC data used in this study are available upon reasonable request to the corresponding author. TNPGN-Active RINEX data set can be accessed by the permission from General Directorate of Land Registry and Cadastre, Department of Mapping at https://www.tusaga-aktif.gov.tr/. The results can be accessed through our institutional repository or by contacting the corresponding author. Additionally, any derived data supporting the findings of this study can be provided upon request. The and the IONOLAB-FFT algorithm code used in this research can be available from the corresponding author on reasonable request for the researchers for further validation and replication of results. The Kp, Ap and Dst indices data is available at https://www-app3.gfz-potsdam.de/kp_index/Kp_ap_since_1932.txt and https://wdc.kugi.kyoto-u.ac.jp/dstdir/.

Declarations

Conflict of interests The authors declare no competing interests.

Ethical approval This manuscript does not report on or involve the use of any animal or human data or tissue.

References

Adil, M. A., Pulinets, S. A., Şentürk, E., Abbasi, A. R., & Budnikov, P. (2022). GNSS atmosphere seismology for equatorial earthquakes: a case study from Central America. *GPS Solutions, 26*, 1-11. https://doi.org/10.1007/s10291-022-01300-9

Amiri-Simkooei, A. R., & Asgari, J. (2012). Harmonic analysis of total electron contents time series: methodology and results. *GPS Solutions, 16*, 77–88. https://doi.org/10.1007/s10291-011-0208-x

Arikan, F., & Yarici, A. (2017). Spectral investigation of traveling ionospheric disturbances: IONOLAB-FFT. *Geodesy and Geodynamics, 8*(5), 297-304. https://doi.org/10.1016/j.geog.2017.05.002

Arikan, F., Erol, C. B., & Arikan, O. (2003). Regularized estimation of vertical total electron content from Global Positioning System data. *Journal of Geophysical Research: Space Physics, 108*(A12), 1-20. https://doi.org/10.1029/2002JA009605

Arikan, F., Erol, C. B., & Arikan, O. (2004). Regularized estimation of vertical total electron content from GPS data for a desired time period. *Radio Science, 39*(6), 1-10. https://doi.org/10.1029/2004RS003061

Arikan, F., Nayir, H., Sezen, U., & Arikan, O. (2008). Estimation of single station interfrequency receiver bias using GPS-TEC. *Radio Science, 43*(4), 1-13. https://doi.org/10.1029/2007RS003785

Bagchi, S., & Mitra, S. K. (2012). *The Nonuniform Discrete Fourier Transform and Its Applications in Signal Processing.* New York: Springer Science+Business Media, LLC.

Belashov, V. Y., & Belashova, E. S. (2015). Nonlinear dynamics of the 3D Alfvén waves in plasma of ionosphere and magnetosphere. *Journal of Atmospheric and Solar-Terrestrial Physics, 136*(B), 150-154. https://doi.org/10.1016/j.jastp.2015.05.005

Borries, C. (2010). The Application of Wavelet Analysis for the Detection of Planetary Wave Type Oscillations in the Ionospheric Total Electron Content. In *Progress in Industrial Mathematics at ECMI 2008* (pp. 305–310). Berlin: Springer.

Bracewell, R. N. (1989). The Fourier Transform. *Scientific American, 260*(6), 86-95.

Budak, C., Karatay, S., Erken, F., & Cinar, A. (2024). Classification of the Ionospheric Disturbances Caused by Geomagnetic and Seismic Activity with K-Nearest Neighbors Algorithm. *Wireless Personal Communications, 134*, 1551–1569. https://doi.org/10.1007/s11277-024-10965-z

Candan, C., Kutay, M., & Ozaktas, H. (2000). The discrete fractional Fourier transform. *IEEE Transactions on Signal Processing, 48*(5), 1329-1337. https://doi.org/10.1109/78.839980

Chernogor, L. F. (2008). Advanced methods of spectral analysis of quasiperiodic wave-like processes in the ionosphere: Specific features and experimental results. *Geomagnetism and Aeronomy, 48*, 652–673 https://doi.org/10.1134/S0016793208050101

Ching-Chou, F., Jhuang, H.-K., Yi-Ying, H., Tsai, T.-C., Lou-Chuang, L., etal. (2025). A Study of Lithosphere–Ionosphere Seismic Precursors from Detecting Gamma-Ray and Total Electron Content Anomalies Prior to the 2018 ML6.2 Hualien Earthquake in Eastern Taiwan. *Remote Sensing, 17*(2), 1-17. https://doi.org/10.3390/rs17020188

Chowdhury, S., Kundu, S., Ghosh, S., Hayakawa, M., Schekotov, A., et al. (2022). Direct and indirect evidence of pre-seismic electromagnetic emissions associated with two large earthquakes in Japan. *Natural Hazards , 112*, 2403–2432. https://doi.org/10.1007/s11069-022-05271-5

Colonna, R., Filizzola, C., Genzano, N., Lisi, M., & Tramutoli, V. (2023). Optimal Setting of Earthquake-Related Ionospheric TEC (Total Electron Content) Anomalies Detection Methods: Long-Term Validation over the Italian Region. *Geosciences,, 13*(5), 1-48. https://doi.org/10.3390/geosciences13050150

Cooley, J. W., Lewis, P. A., & Welch, P. D. (1969). The Fast Fourier Transform and Its Applications. *IEEE Transactions on Education , 12*(1), 27 - 34. https://doi.org/10.1109/TE.1969.4320436

Cravens, T. E., Hamil, O., Renzaglia, A., Ledvina, S. A., & Howard, S. K. (2023). Fourier Analysis of Magnetic Fields in the Ionosphere of Mars. *Journal of Geophysical Research: Space Physics, 128*(4), 1-16. https://doi.org/10.1029/2022JA031044

Crowley, G., Azeem, I., Reynolds, A., Duly, T. M., McBride, P., & Winkler, C. (2016). Analysis of traveling ionospheric disturbances (TIDs) in GPS TEC launched by the 2011 Tohoku earthquake. *Radio Science, 51*(5), 507-514. https://doi.org/10.1002/2015RS005907

Danilov, A. (2013). Ionospheric F-region response to geomagnetic disturbances. *Advances in Space Research, 52*(3), 343-366. https://doi.org/10.1016/j.asr.2013.04.019

Duhamel, P., & Vetterli, M. (1990). Fast fourier transforms: A tutorial review and a state of the art. *Signal Processing, 19*(4), 259-299. https://doi.org/10.1016/0165-1684(90)90158-U

Ackermann, E. R., Villiers, J. P., & Cilliers, P. J. (2011). Nonlinear dynamic systems modeling using Gaussian processes: Predicting ionospheric total electron content over South Africa. *Journal of Geophysical Research: Space Physics, 116*(A10), 1-13. https://doi.org/10.1029/2010JA016375

Eftaxias, K., Balasis, G., Contoyiannis, Y., Papadimitriou, C., Kalimeri, M., et al. (2010). Unfolding the procedure of characterizing recorded ultra low frequency, kHZ and MHz electromagnetic anomalies prior to the L'Aquila earthquake as pre-seismic ones - Part 2. *Natural Hazards and Earth System Sciences, 10*(2), 275–294. https://doi.org/10.5194/nhess-10-275-2010

Fan, Y., Du, X., An, Z., Jun Liu, D. T., & Chen, J. (2015). Earthquake-related Electric Field Changes Observed in the Ionosphere and Ground. *Acta Geophysica, 63*, 679–697. https://doi.org/10.1515/acgeo-2015-0015

GFZ. (1956). *GFZ Helmholtz Centre for Geosciences*. Retrieved 03 12, 2025, from https://www-app3.gfz-potsdam.de/kp_index/Kp_ap_since_1932.txt

Ghafar, M. M., Mohammed, D. H., Salh, H., Dleer, S., Mukhtar, S., & Külahcı, F. (2024). Ionospheric Whispers of the Earth's Tremors: Decoding TEC Mysteries in the East Anatolian Fault Zone. *Geomagnetism and Aeronomy, 64*, 772–780. https://doi.org/10.1134/S0016793223600960

Gousheva, M., Danov, D., Hristov, P., & Matova, M. (2008). Quasi-static electric fields phenomena in the ionosphere associated with pre- and post earthquake effects. *Natural Hazards and Earth System Sciences, 8*(1), 101–107. https://doi.org/10.5194/nhess-8-101-2008

Harrison, R., Aplin, K., & Rycroft, M. (2010). Atmospheric electricity coupling between earthquake regions and the ionosphere. *Journal of Atmospheric and Solar-Terrestrial Physics, 72*(5-6), 376-381. https://doi.org/10.1016/j.jastp.2009.12.004

Hayakawa, M., Nickolaenko, A. P., Galuk, Y. P., & Kudintseva, I. G. (2020). Scattering of extremely low frequency electromagnetic waves by a localized seismogenic ionospheric perturbation: Observation and interpretation. *Radio Science* , *55*(12), 1-26. https://doi.org/10.1029/2020RS007130

Hayakawa, M., Schekotov, A., Izutsu, J., Nickolaenko, A. P., & Hobara, Y. (2023). Seismogenic ULF/ELF Wave Phenomena: Recent Advances and Future Perspectives. *Open Journal of Earthquake Research, 12*, 45-113. https://doi.org/10.4236/ojer.2023.123003

Hayakawa, M., Schekotov, A., Yamaguchi, H., & Hobara, Y. (2023). Observation of Ultra-Low-Frequency Wave Effects in Possible Association with the Fukushima Earthquake on 21 November 2016, and Lithosphere–Atmosphere–Ionosphere Coupling. *Atmosphere, 14*(8), 1-15. https://doi.org/10.3390/atmos14081255

Helmboldt, J. F., Lazio, T. J., Interna, H. T., & Dymond, K. F. (2012). A new technique for spectral analysis of ionospheric TEC fluctuations observed with the very large array VHF system: From QP echoes to MSTIDs. *Radio Science, 47*(4), 1-21. https://doi.org/10.1029/2011RS004787

Hobara, Y., Watanabe, M., Miyajima, R., Kikuchi, H., Tsuda, T., & Hayakawa, M. (2022). On the Spatio-Temporal Dependence of Anomalies in the Atmospheric Electric Field Just around the Time of Earthquakes. *Atmosphere, 13*(10), 1-16. https://doi.org/10.3390/atmos13101619

Igarashi, G., Saeki, S., Takahata, N., & Sumikawa, K. (1995). Ground-Water Radon Anomaly Before the Kobe Earthquake in Japan. *Science* , *269*(5220), 60-61. https://doi.org/10.1126/science.269.5220.6

IGS. (1994). *International GNSS Service*. Retrieved 04 24, 2025, from https://network.igs.org/

IONOLAB. (2007). *Ionosphere Research Laboratory*. Retrieved 03 12, 2025, from www.ionolab.org

Jin, S., Jin, R., & Li, J. H. (2014). Pattern and evolution of seismo-ionospheric disturbances following the 2011 Tohoku earthquakes from GPS observations. *Journal of Geophysical Research: Space Physics, 119*(9), 7914-7927. https://doi.org/10.1002/2014JA019825

Jing, L., Xiaoling, Q., Xuemin, Z., Zhuangkai, W., Chen, Z., & Yu, Z. (2022). Using a Spatial Analysis Method to Study the Seismo-Ionospheric Disturbances of Electron Density Observed by China Seismo-Electromagnetic Satellite. *Frontiers in Earth Science, 10*, 1-20. https://doi.org/10.3389/feart.2022.811658

Kaladze, T., Pokhotelov, O., Shah, H., Khan, M., & Stenflo, L. (2008). Acoustic-gravity waves in the Earth's ionosphere. *Journal of Atmospheric and Solar-Terrestrial Physics, 70*(13), 1607-1616. https://doi.org/10.1016/j.jastp.2008.06.009

Karatay, S. (2020a). Temporal variations of the ionospheric disturbances due to the seasonal variability over Turkey using IONOLAB-FFT algorithm. *Geodesy and Geodynamics, 11*(3), 182-191. https://doi.org/10.1016/j.geog.2019.12.002

Karatay, S. (2020b). Estimation of frequency and duration of ionospheric disturbances over Turkey with IONOLAB-FFT algorithm. *Journal of Geodesy, 94*, 1-24. https://doi.org/10.1007/s00190-020-01416-1

Karatay, S., & Gul, S. E. (2023). Prediction of GPS-TEC on Mw > 5 Earthquake Days Using Bayesian Regularization Backpropagation Algorithm. *IEEE Geoscience and Remote Sensing Letters, 20*, 1-5. https://doi.org/10.1109/LGRS.2023.3262028

Karatay, S., Arikan, F., & Arikan, O. (2010). Investigation of total electron content variability due to seismic and geomagnetic disturbances in the ionosphere. *Radio Science, 45*(5), 1-12. https://doi.org/10.1029/2009RS004313

Karatay, S., Arikan, F., & Arikan, O. (2010). Investigation of total electron content variability due to seismic and geomagnetic disturbances in the ionosphere. *Radio Science, 45*(5), 1-12. https://doi.org/10.1029/2009RS004313

Karatay, S., Arikan, F., & Pirti, A. (2025). patio-temporal evaluation of ionospheric disturbances before, during and after earthquakes using differential rate of TEC (DROT) from GPS measurements. *Environmental Earth Sciences, 84*, 1-15. https://doi.org/10.1007/s12665-025-12216-1

King, C.-Y. (1986). Gas geochemistry applied to earthquake prediction: An overview. *Journal of Geophysical Research: Solid Earth, 91*(B12), 12269-12281. https://doi.org/10.1029/JB091iB12p12269

Koroglu, M., Arikan, F., & Arikan, O. (2020). Time-Frequency Analysis of Ionosphere Disturbances by Using Variational Mode Decomposition. *2020 28th Signal Processing and Communications Applications Conference (SIU).* Gaziantep. https://doi.org/10.1109/SIU49456.2020.9302278

Kowsik, J., Kumar, T., Mounika, G., Ratnam, D. V., & Raghunath, S. (2015). Detection of ionospheric anomalies based on FFT Averaging Ratio (FAR) algorithm. *2015 International Conference on Innovations in Information, Embedded and Communication Systems (ICIIECS).* Coimbatore, India. https://doi.org/10.1109/ICIIECS.2015.7192923

Lean, J. L., Meier, R. R., Picone, J. M., Sassi, F., Emmert, J. T., & Richards, P. G. (2016). Ionospheric total electron content: Spatial patterns of variability. *Journal of Geophysical Research: Space Physics, 121*(10), 10,367-10,402. https://doi.org/10.1002/2016JA023210

Li, M., & Parrot, M. (2013). Statistical analysis of an ionospheric parameter as a base for earthquake prediction. *Journal of Geophysical Research: Space Physics, 118*(6), 3731-3739. https://doi.org/10.1002/jgra.50313

Li, M., Jiang, X., Li, J., Zhang, Y., & Shen, X. (2024). Temporal-spatial characteristics of seismo-ionospheric influence observed by the CSES satellite. *Advances in Space Research, 73*(1), 607-623. https://doi.org/10.1016/j.asr.2023.07.044

Li, Z., Tao, Z., & Cao, L. (2024). Analysis of Ionospheric Anomalies before Earthquakes of Mw6.5 and above in Japan from 2011 to 2022. *Atmosphere, 15*(8), 1-16. https://doi.org/10.3390/atmos15080887

Liperovsky, V. A., Meister, C.-V., Liperovskaya, E. V., Davidov, V. F., & Bogdanov, V. V. (2005). On the possible influence of radon and aerosol injection on the atmosphere and ionosphere before earthquakes. *Natural Hazards and Earth System Sciences, 5*(6), 783–789. https://doi.org/10.5194/nhess-5-783-2005

Liperovsky, V. A., Pokhotelov, O. A., Meister, C. -V., & Liperovskaya, E. V. (2008). Physical models of coupling in the lithosphere-atmosphere-ionosphere system before earthquakes. *Geomagnetism and Aeronomy, 48*, 795–806. https://doi.org/10.1134/S0016793208060133

Liu, J. Y., Chen, Y. I., Chen, C. H., Liu, C. Y., Chen, C. Y., Nishihashi, M., . . . Lin, C. H. (2009). Seismoionospheric GPS total electron content anomalies observed before the 12 May 2008 Mw7.9

Wenchuan earthquake. *Journal of Geophysical Research: Space Physics, 114*(A4), 1-10. https://doi.org/10.1029/2008JA013698

Liu, J., Chen, R., An, J., Wang, Z., & Hyyppa, J. (2014). Spherical cap harmonic analysis of the Arctic ionospheric TEC for one solar cycle. *Journal of Geophysical Research: Space Physics, 119*(1), 601-619. https://doi.org/https://doi.org/10.1002/2013JA019501

Liu, J., Qiao, X., Zhang, X., Wang, Z., Zhou, C., & Zhang, Y. (2022). Using a Spatial Analysis Method to Study the Seismo-Ionospheric Disturbances of Electron Density Observed by China Seismo-Electromagnetic Satellite. *Frontiers in Earth Science, 10*, 1-20. https://doi.org/10.3389/feart.2022.811658

Luhrmann, F., Park, J., Wong, W.-K., Martire, L., Krishnamoorthy, S., & Komjáthy, A. (2025). etection of ionospheric disturbances with a sparse GNSS network in simulated near-real time Mw 7.8 and Mw 7.5 Kahramanmaraş earthquake sequence. *GPS Solutions, 29*, 1-12. https://doi.org/10.1007/s10291-024-01808-2

Marchetti, D., De Santis, A., Jin, S., A. Campuzano, S., Cianchini, G., & Piscini, A. (2020). Co-Seismic Magnetic Field Perturbations Detected by Swarm Three-Satellite Constellation. *Remote Sensing, 12*(7), 1-21. https://doi.org/10.3390/rs12071166

Mikumo, T., & Watada, S. (2009). Acoustic-Gravity Waves from Earthquake Sources. In *Infrasound Monitoring for Atmospheric Studies* (pp. 263–279). Dordrecht: Springer.

Molchanov, O. A., Hayakawa, M., & Rafalsky, V. A. (1995). Penetration characteristics of electromagnetic emissions from an underground seismic source into the atmosphere, ionosphere, and magnetosphere. *Journal of Geophysical Research: Space Physics, 100*(A2), 1691-1712. https://doi.org/10.1029/94JA02524

Naaman, S., Alperovich, L. S., Wdowinski, S., Hayakawa, M., & Calais, E. (2001). Comparison of simultaneous variations of the ionospheric total electron content and geomagnetic field associated with strong earthquakes. *Natural Hazards and Earth System Sciences, 1*(1/2), 53–59. https://doi.org/10.5194/nhess-1-53-2001, 2001

Nayir, H., Arikan, F., Arikan, O., & Erol, C. B. (2007). Total Electron Content Estimation with Reg-Est. *Journal of Geophysical Research: Space Physics, 112*(A11), 1-11. https://doi.org/10.1029/2007JA012459

Nikolopoulos, D., Cantzos, D., Alam, A., Dimopoulos, S., & Petraki, E. (2024). Electromagnetic and Radon Earthquake Precursors. *Geosciences, 14*(10), 1-42. https://doi.org/10.3390/geosciences14100271

Novikov, V. A., & Sorokin, V. M. (2024). Electromagnetic Trigger Effects in the Ionosphere–Atmosphere–Lithosphere System and Their Possible Use for Short-Term Earthquake Forecasting. *Izvestiya, Physics of the Solid Earth, 60*, 879–890. https://doi.org/10.1134/S1069351324700800

Olson, T. (2017). The Discrete Fourier Transform. In *Applied Fourier Analysis* (pp. 75–120). New York: Birkhäuser.

Omori, Y., Yasuoka, Y., Nagahama, H., Kawada, Y., Ishikawa, T., Tokonami, S., & Shinogi, M. (2007). Anomalous radon emanation linked to preseismic electromagnetic phenomena. *Natural Hazards and Earth System Sciences, 7*(5), 629–635. https://doi.org/10.5194/nhess-7-629-2007

Ondoh, T. (2000). Seismo-ionospheric phenomena. *Advances in Space Research, 26*(8), Advances in Space Research. https://doi.org/10.1016/S0273-1177(99)01215-6

Perfetti, N., Taddia, Y., & Pellegrinelli, A. (2025). Monitoring of Ionospheric Anomalies Using GNSS Observations to Detect Earthquake Precursors. *Remote Sensing, 17*(2), 1-22. https://doi.org/10.3390/rs17020338

Pulinets, S. A. (2004). Ionospheric Precursors of Earthquakes: Recent Advances in Theory and Practical Applications. *Terrestrial Atmospheric and Oceanic Sciences, 15*(3), 413-435. https://doi.org/10.3319/TAO.2004.15.3.413(EP)

Pulinets, S., & Ouzounov, D. (2011). Lithosphere–Atmosphere–Ionosphere Coupling (LAIC) model – An unified concept for earthquake precursors validation. *Journal of Asian Earth Sciences, 41*(4/5), 371-382. https://doi.org/10.1016/j.jseaes.2010.03.005

Qingshan Ruan, Yuan, X., Liu, H., & Ge, S. (2023). Study on co-seismic ionospheric disturbance of Alaska earthquake on July 29, 2021 based on GPS TEC. *Scientific Reports, 13*, 1-14. https://doi.org/10.1038/s41598-023-37374-9

Raghunath, S., & Ratnam, D. V. (2015). Detection of Low-Latitude Ionospheric Irregularities From GNSS Observations. *IEEE Journal of Selected Topics in Applied Earth Observations and Remote Sensing , 8*(11), 5171 - 5176. https://doi.org/10.1109/JSTARS.2015.2496201

Rapoport, Y., Gotynyan, O., Ivchenko, V., Kozak, L., & Parrot, M. (2004). Effect of acoustic-gravity wave of the lithospheric origin on the ionospheric F region before earthquakes. *Physics and Chemistry of the Earth, Parts A/B/C, 29*(4-9), 607-616. https://doi.org/10.1016/j.pce.2003.10.006

Reddy, C., Sunil, A., González, G., Shrivastava, M. N., & Moreno, M. (2015). Near-field co-seismic ionospheric response due to the northern Chile Mw 8.1 Pisagua earthquake on April 1, 2014 from GPS observations. *Journal of Atmospheric and Solar-Terrestrial Physics, 134*, 1-8. https://doi.org/10.1016/j.jastp.2015.09.006

Rideout, W., & Coster, A. (2006). Automated GPS processing for global total electron content data. *GPS Solutions, 10*, 219–228. https://doi.org/10.1007/s10291-006-0029-5

Ruan, Q., Liu, H., Yuan, X., Ge, S., Cheng, X., & Wang, W. (2025). Analysis of co-seismic ionospheric disturbance of the Qinghai Mw 7.4 earthquake on May 21, 2021. *International Journal of Remote Sensing , 46*(5), 2233-2253. https://doi.org/10.1080/01431161.2025.2450563

Saleem, H., & Shan, S. A. (2020). Theoretical models for unstable IAWs and nonlinear structures in the upper ionosphere. *Reviews of Modern Plasma Physics, 4*, 1-42. https://doi.org/10.1007/s41614-019-0038-9

Sardón, E., Rius, A., & Zarraoa, N. (1994). Estimation of the transmitter and receiver differential biases and the ionospheric total electron content from Global Positioning System observations. *Radio Science, 29*(3), 577-586. https://doi.org/10.1029/94RS00449

Sezen, U., Arikan, F., Arikan, O., Ugurlu, O., & Sadeghimorad, A. (2013). Online, automatic, near-real time estimation of GPS-TEC: IONOLAB-TEC. *Space Weather, 11*(5), 297-305. https://doi.org/10.1002/swe.20054

Shi, K., Ding, H., Guo, J., & Yu, T. (2021). Refined seismic-ionospheric effects: case study of Mw 8.2 Chiapas earthquake on September 7, 2017. *GPS Solutions, 25*, 1-12. https://doi.org/10.1007/s10291-021-01129-8

Siddiqui, T. A., Yamazaki, Y., Stolle, C., Maute, A., Laštovička, J., et al. (2021). Understanding the Total Electron Content Variability Over Europe During 2009 and 2019 SSWs. *Journal of Geophysical Research: Space Physics, 126*(9), 1-22. https://doi.org/10.1029/2020JA028751

Skeberis, C., Zaharis, Z., Xenos, T., Spatalas, S., Arabelos, D., & Contadakis, M. (2015). Time–frequency analysis of VLF for seismic-ionospheric precursor detection: Evaluation of Zhao-Atlas-Marks and Hilbert-Huang Transforms. *Physics and Chemistry of the Earth, Parts A/B/C, 85–86*, 174-184. https://doi.org/10.1016/j.pce.2015.02.006

Solomon, S. C., Qian, L., & Mannucci, A. J. (2018). Ionospheric Electron Content During Solar Cycle 23. *Journal of Geophysical Research: Space Physics, 123*(6), 5223-5231. https://doi.org/10.1029/2018JA025464

Sripathi, S., Singh, R., Tiwari, P., & Kumar, M. R. (2020). On the Co-Seismic Ionospheric Disturbances (CIDs) in the Rapid Run Ionosonde Observations Over Allahabad Following Mw 7.8 Nepal Earthquake on April 25, 2015. *Journal of Geophysical Research: Space Physics, 125*(1), 1-16. https://doi.org/10.1029/2019JA027001

Su, Y.-C., & Sha, J. (2022). A Study of Possible Correlations between Seismo-Ionospheric Anomalies of GNSS Total Electron Content and Earthquake Energy. *Remote Sensing, 14*(5), 1-22. https://doi.org/10.3390/rs14051155

Sundararajan, D. (2001). *Discrete Fourier Transform, the: Theory, Algorithms and Applications.* Singapore: World Scientific Pub Co Inc .

Swati, P., Singh, B., Pundhir, D., Sinha, A. K., Rao, K. M., Guha, A., & Hobara, Y. (2020). Ultra-low frequency (ULF) magnetic field emissions associated with some major earthquakes occurred in Indian Subcontinent. *Journal of Atmospheric and Solar-Terrestrial Physics, 211*, 1-19. https://doi.org/10.1016/j.jastp.2020.105469

Tachema, A. (2024). Identifying pre-seismic ionospheric disturbances using space geodesy: A case study of the 2011 Lorca earthquake (Mw 5.1), Spain. *Earth Science Informatics, 17*, 2055–2071. https://doi.org/10.1007/s12145-024-01272-z

Trique, M., Richon, P., Perrier, F., Avouac, J. P., & Sabroux, J. C. (1999). Radon emanation and electric potential variations associated with transient deformation near reservoir lakes. *Nature , 399*, 137–141. doi:https://doi.org/10.1038/20161

Tritakis, V., Mlynarczyk, J., Contopoulos, I., Kubisz, J., Christofilakis, V., et al. (2024). Extremely Low Frequency (ELF) Electromagnetic Signals as a Possible Precursory Warning of Incoming Seismic Activity. *Atmosphere, 15*(4), 1-15. https://doi.org/10.3390/atmos15040457

USGS. (1879). *United States Geological Survey*. Retrieved 11 05, 2025, from https://www.usgs.gov/programs/earthquake-hazards/earthquakes

Wang, J., & Morton, Y. T. (2015). High-Latitude Ionospheric Irregularity Drift Velocity Estimation Using Spaced GPS Receiver Carrier Phase Time–Frequency Analysis. *IEEE Transactions on Geoscience and Remote Sensing, 53*(11), 6099-6113. https://doi.org/10.1109/TGRS.2015.2432014

Wang, J.-S., Chen, Z., & Huang, C.-M. (2014). A method to identify aperiodic disturbances in the ionosphere. *Annales Geophysicae, 32*(5), 563–569. https://doi.org/10.5194/angeo-32-563-2014

Wang, Z. (1984). Fast algorithms for the discrete W transform and for the discrete Fourier transform. *EEE Transactions on Acoustics, Speech, and Signal Processing, 32*(4), 803-816. https://doi.org/10.1109/TASSP.1984.1164399

WDC. (1957). *WDC for Geomagnetism, Kyoto*. Retrieved 03 12, 2025, from https://wdc.kugi.kyoto-u.ac.jp///dstae///wwwtmp/WWW_dstae03340870.dat

Yuen, P. C., & Roelofs, T. H. (1966). Diurnal variation of the ionospheric total electron content. *Journal of Geophysical Research, 71*(3), 849-854. https://doi.org/10.1029/JZ071i003p00849

Yuen, P., & Roelofs, T. (1967). Seasonal variations in ionospheric total electron content. *Journal of Atmospheric and Terrestrial Physics, 29*(3), 321-326. https://doi.org/10.1016/0021-9169(67)90203-6